Lipid hydroperoxides promote sarcopenia through carbonyl stress

Hiroaki Eshima,[1-3,#] Justin L. Shahtout,[1,4,#] Piyarat Siripoksup,[1,4] MacKenzie J. Pearson,[5] Ziad S. Mahmassani,[1,2,4] Patrick J. Ferrara,[1,2,6] Alexis W. Lyons,[1] J. Alan Maschek,[1,6,7] Alek D. Peterlin,[1,6] Anthony R. P. Verkerke,[1,6] Jordan M. Johnson,[1,6] Anahy Salcedo,[1] Jonathan J. Petrocelli,[1,4] Edwin R. Miranda,[1,2] Ethan J. Anderson,[8] Sihem Boudina,[1,2,6] Qitao Ran,[9] James E. Cox,[1,7,10] Micah J. Drummond,[1,2,4] Katsuhiko Funai,[1,2,4,6*]

[1]Diabetes & Metabolism Research Center, University of Utah, Salt Lake City, Utah, USA

[2]Molecular Medicine Program, University of Utah, Salt Lake City, Utah, USA

[3]Department of International Tourism, Nagasaki International University, Sasebo, Nagasaki, Japan

[4]Department of Physical Therapy & Athletic Training, University of Utah, Salt Lake City, Utah, USA

[5]Sciex, Framingham, MA, USA

[6]Department of Nutrition & Integrative Physiology, University of Utah, Salt Lake City, Utah, USA

[7]Metabolomics Core Research Facility, University of Utah, Salt Lake City, Utah, USA

[8]Fraternal Order of Eagles Diabetes Research Center, University of Iowa, Iowa City, Iowa, USA

[9]Department of Cell Systems and Anatomy, University of Texas Health Science Center at San Antonio, San Antonio, Texas, USA

[10]Department of Biochemistry, University of Utah, Salt Lake City, Utah, USA

[#]The authors contributed equally.

*Corresponding Author:

Katsuhiko Funai, Ph.D.

Diabetes & Metabolism Research Center

15 N 2030 E, Salt Lake City, UT 84112

Phone: (801) 585-1781

Fax: (801) 585-0701

Email: kfunai@utah.edu

Summary

Reactive oxygen species (ROS) accumulation is a cardinal feature of skeletal muscle atrophy. ROS refers to a collection of radical molecules whose cellular signals are vast, and it is unclear which downstream consequences of ROS are responsible for the loss of muscle mass and strength. Here we show that lipid hydroperoxides (LOOH) are increased with age and disuse, and the accumulation of LOOH by deletion of glutathione peroxidase 4 (GPx4) is sufficient to augment muscle atrophy. LOOH promoted atrophy in a lysosomal-dependent, proteasomal-independent manner. In young and old mice, genetic and pharmacologic neutralization of LOOH or their secondary reactive lipid aldehydes robustly prevented muscle atrophy and weakness, indicating that LOOH-derived carbonyl stress mediate age- and disuse-induced muscle dysfunction. Our findings provide novel insights for the role of LOOH in sarcopenia including a therapeutic implication by pharmacologic suppression.

Introduction

Loss of muscle mass and function with age is detrimental to health and quality of life [1, 2]. Sarcopenia, muscle atrophy and weakness with aging, is due to a combination of inactivity, injury, surgery, and biological consequences of aging [3, 4]. A pharmacologic therapy for muscle loss does not exist, and current diet or exercise therapeutic approaches are often ineffective or unfeasible. Oxidative stress has been implicated in muscle atrophy by accelerating proteolysis [5, 6], but the exact mechanism by which reactive oxygen species (ROS) contributes to the decrease in muscle mass and strength is not well understood.

Lipid hydroperoxide (LOOH) is a class of ROS molecules that has been implicated in cell damage, particularly as a trigger to induce ferroptosis, a non-apoptotic form of regulated cell death [7, 8]. Lipid peroxidation is initiated by prooxidants such as hydroxyl radicals attacking the carbon-carbon double bond in fatty acids, particularly the polyunsaturated fatty acids (PUFAs) containing phospholipids [9]. Lipid radicals (L•) created by this reaction rapidly reacts with oxygen to form a lipid peroxy-radical which subsequently reacts with another lipid to produce L• and LOOH, the former propagating lipid peroxidation. LOOH is the primary product of lipid peroxidation that forms secondary reactive lipid aldehydes such as 4-hydroxynonenal (4-HNE) and malondialdehyde (MDA), inducing carbonyl stress with high reactivity against biological molecules to promote cellular toxicity. The intracellular level of LOOH is endogenously suppressed by glutathione peroxidase 4 (GPx4) that catalyzes the reaction by which LOOH is reduced to its nonreactive hydroxyl metabolite [10].

Despite the evidence for the role of LOOH-mediated cell damage and cell death, the biological consequence of LOOH accumulation in skeletal muscle is not well

understood [11, 12]. Below we provide evidence that LOOH mediates the loss of muscle mass and function associated with sarcopenia. An increase in muscle LOOH was a common feature with aging and disuse, and accumulation of LOOH in vitro and in vivo augmented muscle atrophy. We further show that genetic or pharmacologic suppression of LOOH and their reactive lipid aldehydes is sufficient to prevent disuse-induced muscle atrophy in young and old mice.

Results

We first evaluated the changes in skeletal muscle LOOH with aging. In humans and in mice, aging promoted a reduction in the expression of GPx4 in skeletal muscle (Fig. 1A&B). To examine the changes in skeletal muscle LOOH landscape with age, we performed a comprehensive oxidolipidomic analysis in muscle samples from young (4 months) and old (20 months) mice (Fig. 1C&D). We detected over 300 species of oxidized lipids with an effect distribution that was highly class-dependent. Among these, age had the most robust effect on oxidized phosphatidylethanolamine (Fig. 1C, red), a class of lipids that have been implicated as a potential lipid signal to induce ferroptosis [13]. Among the top ten oxidized lipid species whose abundance was most robustly increased with age, six of them were oxidized phosphatidylethanolamine (Figure 1D), and they were substantially more highly abundant compared to other oxidized lipids. LOOH can be indirectly assessed by quantifying lipid aldehyde adducts such as 4-hydroxynonenal (4-HNE) and malondialdehyde (MDA). We confirmed increased muscle 4-HNE and MDA with age (Fig. 1E-G).

Disuse promoted by inactivity, injury, or surgery is a major contributor to age-associated decline in muscle mass and function. Disuse also promotes skeletal muscle atrophy that is likely contributed by ROS [5]. To model disuse atrophy, mice underwent

a hindlimb unloading (HU) procedure as previously described [14, 15] (Supplemental Fig. S1A-J). As expected, HU induced muscle atrophy and weakness (Supplemental Fig. S1D&E) concomitant to reduction in body and lean mass (Supplemental Fig. S1B&C). Disuse robustly elevated muscle LOOH levels (Supplemental Fig. S1F&G) without significant changes in mitochondrial bioenergetics (Supplemental Fig. S1H-J). An increase in muscle LOOH preceded atrophy (Supplemental Fig. S1D&F), consistent with the notion that LOOH may trigger mechanisms to promote loss of muscle mass.

Next, we tested our hypothesis that LOOH contributes to muscle atrophy using C2C12 myotubes (Fig. 2A). Lentivirus-mediated knockdown (KD) of GPx4 increased LOOH and markers of ferroptosis concomitant with a decrease in myotube diameter (Fig. 2B-I). We also recapitulated these findings with erastin (a system X_c^- inhibitor that suppresses glutathione synthesis) (Fig. 2B&C and Supplemental Fig. S2A-E) and RSL3 (GPx4 inhibitor) (Fig. 2B&C and Supplemental Fig. S2F-I), commonly used acute pharmacological interventions to elevate intracellular LOOH. These data support the idea that LOOH reduces myotube size in a cell-autonomous manner.

We then translated these findings in vivo with global heterozygous GPx4 knockout mice ($GPx4^{+/-}$). Germline deletion of GPx4 is embryonically lethal [16], but $GPx4^{+/-}$ mice appear normal and do not have an observable muscle phenotype at baseline [10, 17]. We studied 4 months (young) and 20 months (old) $GPx4^{+/-}$ and wildtype littermates with or without HU (Supplemental Fig. S3A-D). In young mice, GPx4 haploinsufficiency augmented the loss in muscle mass induced by HU (Fig. 3A and Supplemental Fig. S3E). However, muscle masses between old $GPx4^{+/-}$ and wildtype mice were not different. We interpret these findings to mean that disuse in old mice promotes an increase in LOOH that has already reached a maximally effective threshold with age

such that GPx4 deletion had no further effect. In support of this, we saw no differences in 4-HNE or MDA levels between old GPx4$^{+/-}$ and wildtype mice (Fig. 3B and Supplemental Fig. S3F&G). GPx4 haploinsufficiency did not alter force-generating capacity (Fig. 3C and Supplemental Fig. S3H-J).

Because GPx4 is expressed globally, we also studied mice with skeletal muscle-specific tamoxifen-inducible GPx4 knockout (GPx4-MKO) (Fig. 3D and Supplemental Fig. S4A) [18]. Consistent with GPx4+/- mice, GPx4-MKO mice were also more prone to developing disuse-induced skeletal muscle atrophy (Fig. 3E&F and Supplemental Fig. S4B-F) concomitant to elevated LOOH (Fig. 3G and Supplemental Fig. S4G&H), suggesting that loss of GPx4 in muscle augments atrophy in a cell-autonomous manner. Histological analyses revealed that reduced muscle mass was consistent with reduced cross-sectional area of myofibers regardless of fiber-type compositions (Fig. 3H&I and Supplemental Fig. S4I&J). These data implicate that LOOH directly reduces muscle cell size in vivo.

GPx4 primarily neutralizes LOOH but it also exhibits some activity towards other peroxides [19]. To confirm that the effects of GPx4 deletion to promote atrophy is specific to LOOH, we diminished the ability of cells to incorporate PUFAs into phospholipids by deleting lysophosphatidylcholine acyltransferase 3 (LPCAT3) [20-22]. LPCAT3 is an enzyme of Lands cycle that preferentially acylates lysophospholipids with PUFAs, and thus an essential component of ferroptosis [13]. Indeed, LPCAT3 KD rescued the increase in 4-HNE induced by GPx4 KD (Fig. 4A and Supplemental Fig. S5A). Remarkably, deletion of LPCAT3 KD completely restored the reduction in myotube diameter induced by GPx4 KD (Fig. 4D&E). Similarly, LPCAT3 deletion also prevented LOOH and cell death induced by erastin (Fig. 5F-H and Supplemental Fig.

S5B&C). These findings indicate that muscle atrophy induced by loss of GPx4 or erastin treatment is due to the accumulation of LOOH and not other peroxides.

What is the mechanism by which LOOH promotes muscle atrophy? C2C12 myotubes were pretreated with Bafilomycin A1 (BafA1) or MG132 prior to erastin incubation to determine whether LOOH increases protein degradation in a lysosomal- or proteasomal-dependent manner, respectively. Erastin-induced reduction in myotube diameter was suppressed with BafA1, but not with MG132 (Fig. 5A&B and Supplemental Fig. S6A), suggesting that the lysosome mediates protein degradation by LOOH [23]. We also reproduced these findings with RSL3 treatment (Supplemental Fig. S6B&C). How does LOOH, a lipid molecule, promote lysosomal-degradation? Upstream of the lysosome, autophagosome formation is mediated by a lipidation of LC3 by ATG3 [24]. Thus, we hypothesized that LOOH may affect the lipidation of LC3. Indeed, GPx4 KD drastically reduced the protein content of p62, LC3-I and LC3-II (Fig. 5C and Supplemental Fig. S6D-H), potentially suggesting that LOOH may accelerate lysosomal degradation by affecting LC3 lipidation. To test this possibility, we performed a targeted deletion of ATG3 in vitro. Indeed, ATG3 KD completely rescued the reduction in myotube diameter induced by GPx4 KD (Fig. 5D&E and Supplemental Fig. S6I-L).

Leveraging these findings, we generated mice with skeletal muscle-specific tamoxifen-inducible ATG3 knockout (ATG3-MKO) (Fig. 6A&B and Supplemental Fig. S7A&B) and studied them with or without HU (Supplemental Fig. S7C-E). Loss of muscle ATG3 was protective from disuse-induced atrophy (Fig. 6C and Supplemental Fig. S7F) and weakness (Fig. 6D and Supplemental Fig. S7G) which can be explained by greater myofiber cross-sectional area (Fig. 6E&D and Supplemental Fig. S7I). Thus,

178 suppression of autophagy is sufficient to attenuate disuse-induced muscle atrophy and
179 weakness.
180
181 We initially hypothesized that lysosomal-degradation mediates LOOH-induced protein
182 degradation to contribute to muscle atrophy. However, further assessment of muscle
183 LOOH illuminated a more complex interaction between the lysosome and LOOH [25,
184 26]. Unexpectedly, quantification of 4-HNE revealed that inhibition of the autophagy-
185 lysosome axis by ATG3 deletion or BafA1 was sufficient to inhibit LOOH induced by
186 GPx4 deletion, erastin, or RSL3 (Fig. 7A-D and Supplemental Fig. S8A-D). These
187 findings suggest that the autophagy-lysosome axis is essential for LOOH amplification,
188 in addition to its potential role in mediating protein degradation downstream. Indeed,
189 immunofluorescence experiments revealed that 4-HNE is highly co-localized to LAMP2
190 (Fig. 7E and Supplemental Fig. S8E), consistent with the notion that the lysosome is
191 necessary for LOOH propagation. To support this idea, an increase in LOOH by
192 hydrogen peroxide or carmustine (agents that increase pan oxidative stress without
193 acting on GPx4 directly) was completely inhibited by lysosomal inhibition (Fig. 7F-H
194 and Supplemental Fig. S8F&G). Together, these observations suggest that the
195 propagation of LOOH may be mediated by the lysosome (Supplemental Fig. S8H).
196
197 Inhibition of autophagy suppressed lysosomal-degradation and LOOH to attenuate
198 muscle atrophy. We next tested whether suppression of LOOH would be sufficient to
199 ameliorate skeletal muscle atrophy. We studied young (4 months) and old (20 months)
200 global GPx4-overexpressing (GPx4Tg) mice [27] with or without HU (Supplemental Fig.
201 S9A-E). Strikingly, both young and old GPx4Tg mice were resistant to disuse-induced
202 muscle atrophy (Fig. 8A and Supplemental Fig. 9F&G). Perhaps even more impactful
203 was the effect of GPx4 overexpression on skeletal muscle force-generating capacity

such that, in both young and old, GPx4 overexpression robustly protected mice from muscle weakness induced by HU (Fig. 8B and Supplemental Fig. S9H-J). These findings are in contrast to our experiments in GPx4$^{+/-}$ mice where muscle mass phenotype was only present in the young mice (Fig. 3A) and no phenotype on muscle strength (Fig. 3C). Consistent with the notion that GPx4 overexpression acts on LOOH, HU-induced increase in 4-HNE was completely suppressed in GPx4Tg mice (Fig. 8C and Supplemental Fig. S9K). We also found that the protection from muscle atrophy was explained by greater myofiber cross-sectional area regardless of fiber-type (Fig. 8D&E and Supplemental Fig. S9L&M).

Next, we explored opportunities to pharmacologically suppress LOOH to prevent muscle atrophy. Ferrostatin-1 inhibits the propagation of lipid peroxidation and is widely used to study LOOH [28, 29]. Indeed, incubation of cells with ferrostatin-1 was sufficient to suppress LOOH induced by GPx4 KD (Fig. 8F and Supplemental Fig. S10A) concomitant with protection from myotube atrophy (Fig. 8G&H and Supplemental Fig. S10B&C). Nevertheless, ferrostatin-1 is currently not an FDA approved drug with uncertainty surrounding safety. Thus, we tested L-carnosine, a dipeptide composed of beta-alanine and L-histidine that has the ability to scavenge reactive lipid aldehydes formed from LOOH [30, 31]. Rather than acting to suppress the lipid peroxidation process, L-carnosine binds to reactive lipid aldehydes to neutralize carbonyl stress. Similar to ferrostatin-1, L-carnosine was sufficient to suppress 4-HNE and rescue cell death induced by GPx4 KD (Supplemental Fig. S10D-F) or erastin (Supplemental Fig. S10G-I). Leveraging these data, we performed a preclinical trial for L-carnosine provided in drinking water ad lib (80 mM) in young wildtype C57BL6/J mice. L-carnosine treatment did not alter body mass, body composition, food intake, and water intake (Supplemental Fig. S11A-D), and successfully suppressed muscle 4-

HNE induced by HU (Supplemental Fig. S11E&F). Remarkably, mice provided with L-carnosine were partly protected from disuse-induced muscle atrophy (Supplemental Fig. S11G).

In humans, L-carnosine is rapidly degraded by a circulating carnosinase [32] that may render oral carnosine treatment ineffective. In contrast, N-acetylcarnosine has a longer half-life and may be a more effective reagent in humans thus improving its translational potential. Similar to ferrostatin-1 and L-carnosine, N-acetylcarnosine also prevented 4-HNE and cell death induced by GPx4 KD (Supplemental Fig. S12A-C) or erastin (Supplemental Fig. S12D-F). Thus, we proceeded with a preclinical trial for N-acetylcarnosine in drinking water (80 mM, Fig. 9A) in young (4 months, C57BL6/J; Jax colony) and old (20 months, C57BL/6; NIA rodent colony) wildtype mice. Similar to L-carnosine treatment, N-acetylcarnosine did not alter body mass, body composition, food intake, or water intake (Supplemental Fig. S13A-E), and successfully suppressed muscle 4-HNE (Fig. 9B and Supplemental Fig. S13F&G). Strikingly, similar to our findings in GPx4Tg mice, N-acetylcarnosine ameliorated muscle atrophy (Fig. 9C and Supplemental Fig. S13H) and weakness (Fig. 9D and Supplemental Fig. S13I-K) in both young and old mice. Protection from muscle atrophy was similarly explained by greater myofiber cross-sectional area regardless of fiber-type (Fig. 9E&F and Supplemental Fig. S13L&M).

Discussion

The current findings demonstrate a novel mechanism that indicate LOOH as the key downstream molecule by which oxidative stress promotes muscle atrophy and weakness. Skeletal muscle LOOH was robustly upregulated with aging and disuse, and genetic or pharmacologic neutralization of LOOH and their secondary reactive lipid

aldehydes was sufficient to rescue muscle atrophy and weakness. In particular, N-acetylcarnosine treatment shows a potent effect in preserving muscle mass and strength with disuse in both young and old mice, informing the potential trial to utilize this compound to ameliorate loss of muscle function in humans.

During the preparation of this manuscript, Van Remmen and colleagues published a complementary study demonstrating that liproxstatin-1 can suppress denervation-induced skeletal muscle atrophy [33]. Denervation and HU elicits different but overlapping response in myofibers, and our studies demonstrate that their effects to drive skeletal muscle atrophy might converge on lipid peroxidation. Like ferrostatin-1, liproxstatin-1 acts to suppress the propagation of lipid peroxidation rather than acting directly on LOOH. Nevertheless, in vivo liproxstatin-1 treatment was highly effective in suppressing denervation-induced LOOH as well as reactive lipid aldehydes 4-HNE, suggesting that targeting lipid peroxidation is likely an equally effective strategy to suppress LOOH production in skeletal muscle. Conversely, our data with GPx4 overexpression and N-acetylcarnosine treatment indicate that the effect of lipid peroxidation to promote muscle atrophy is mediated by LOOH and their lipid reactive aldehydes. Neither liproxstatin-1 nor ferrostatin-1 are currently FDA approved, but it is worthwhile to consider these drugs along with N-acetylcarnosine as potential therapeutics to treat muscle atrophy.

Sarcopenia is an age-associated decline in muscle mass and strength, that occurs due to a combination of inactivity, injury, and/or surgery, in addition to the biological consequences of aging itself. In the current study, mice were studied at 4 or 20 months of age. While not statistically compared directly (these experiments were not performed side-by-side), skeletal muscle mass at 20 months of age was not significantly lower

compared to those at 4 months of age. Thus, the current data is unclear whether targeting LOOH prevents the loss of muscle mass due to the biological effect of aging in the absence of HU. We chose to study mice with 20 months of age for two reasons. First, mice greater than 20 months of age do not tolerate the HU intervention well, often resulting in their inability to consume food or water. Because disuse is an integral component of human aging, we wanted to study how muscles from old mice respond to disuse. This therefore compromised our ability to study sarcopenia without disuse. Second, while muscle mass was not diminished at 20 months of age, skeletal muscle force-generating capacity was lower in 20 months old mice compared to the 4 months old mice, particularly in the extensor digitorum longus (EDL) muscles. In GPx4Tg mice, age-associated decrease in muscle strength (in non-HU mice) appeared to be rescued, while short-term treatment with N-acetylcarnosine had no effect. We are currently following up on these results with a long-term treatment of N-acetylcarnosine in 24 months old mice to see if such intervention might alleviate the loss of muscle mass and strength associated with age in absence of the HU intervention.

We initially set out to investigate the role of LOOH in age- and disuse-induced skeletal muscle atrophy, while measuring force-generating capacity as a secondary outcome. However, in all experimental models in which accumulation of muscle LOOH was suppressed (young and old GPx4Tg mice, young and old mice with N-acetylcarnosine, and young ATG3-MKO mice), force-generating capacity (i.e., specific force normalized to cross-sectional area) was more robustly rescued compared to skeletal muscle mass. This suggests the role of LOOH to induce muscle weakness independent of muscle atrophy, and likely independent of muscle protein degradation. While out of the scope for the current study, it would be important to determine whether reactive lipid aldehydes induced by aging or disuse preferentially bind to enzymes of skeletal muscle

contraction to compromise their activities. As described in the previous paragraph, aging promoted muscle weakness prior to atrophy. Similarly, muscle atrophy induced by cancer cachexia is also preceded by muscle weakness [34]. Thus, these observations highlight the need to better study the mechanisms that regulate force-generating capacity independent of muscle mass.

In conclusion, we provide evidence that LOOH contributes to the loss of muscle mass and strength associated with age and disuse. Neutralization of LOOH, particularly their reactive lipid aldehyde byproducts, attenuates muscle atrophy and weakness. The mechanisms by which LOOH contributes to these phenotypes are not entirely clear, but they include protein degradation mediated by the autophagy-lysosomal axis, as well as loss in the force-generating capacity that is likely mediated by carbonyl stress. Last, but not least, these promising observations inform a potential clinical trial to test the efficacy of N-acetylcarnosine treatment in ameliorating muscle atrophy in humans.

Methods

Key Resources

REAGENT or RESOURCE	SOURCE	IDENTIFIER
Antibodies		
4-Hydroxynonenal (4-HNE)	Abcam	Ab48506
Actin	Millipore Sigma	A2066
Alexa Fluor 647-conjugated secondary (Goat Anti-Mouse)	Invitrogen	A21242
Alexa Fluor 568-conjugated secondary (Donkey Anti-Mouse)	Abcam	Ab175472
Alexa Fluor 555-conjugated secondary (Goat Anti-Mouse)	Invitrogen	A21426
Alexa Fluor 488-conjugated secondary (Donkey Anti-Rabbit)	Abcam	Ab150073
Alexa Fluor 488-conjugated secondary (Goat Anti-Mouse)	Invitrogen	A21121
GAPDH	Cell Signaling Technology	14C10
GPx4	Abcam	Ab125066
Lamp-2	Novus	NB300-591
LC3B	Cell Signaling Technology	83506
Myosin Heavy Chain Type I	DSHB	BA.D5
Myosin Heavy Chain Type IIA	DSHB	SC.71
Myosin Heavy Chain Type IIB	DSHB	BF.F3
P62	Abcam	Ab56416
Biological samples		
Human Muscle Biopsy Samples	Tanner et al. 2015 Reidy et al. 2017	N/A
Chemicals, peptides, and recombinant proteins		
4% Paraformaldehyde	Thermo	J19943-K2
Amplex Red Reagent	Invitrogen	A12222
Auranofin	Sigma Aldrich	A6733
ADP	Sigma Aldrich	A5285
BaFA1	Millipore Sigma	SML1661
Bovine Serum Albumin	Sigma Aldrich	A7030
Carmustine (BCNU)	Sigma Aldrich	C0400
DAPI	Invitrogen	D1306
ECL	PerkinElmer	104001EA
Erastin	Millipore Sigma	E7781
Ferrostatin-1	Millipore Sigma	SML0583
Ketamine	MWI Animal Health	501072
L-carnosine	Millipore Sigma	C9625
Malate	Sigma Aldrich	M7397
Mini-PROTEAN TGX Gels	BioRad	4561086
Mouse IgG Blocking Reagent	Vector Laboratories	MKB-2213
N-acetylcarnosine	Cayman Chemical	18817
Opti-MEM	Gibco	31985
Protease Inhibitor Cocktail	Thermo Scientific	78446

Pyruvate	Sigma Aldrich	P2256
RSL3	Millipore Sigma	SLM2234
Succinate	Sigma Aldrich	S3674
Sunflower Oil	Sigma Aldrich	S5007
SYBR Green	Thermo Scientific	A25776
Tamoxifen	Sigma Aldrich	T5648
Trypan Blue	Sigma Aldrich	T8154
TRIzol	Thermo Scientific	15596018
Triton X-100	Sigma Aldrich	A16046-AE
Xylazine	MWI Animal Health	510024
Critical commercial assays		
Pierce BCA Protein Assay Kit	Thermo Scientific	23227
iScript cDNA Synthesis Kit	BioRad	1708891
MDA Lipid Peroxidation Assay	Abcam	Ab118970
Deposited data		
Experimental models: Cell lines		
C2C12 Myoblasts	ATCC	CRL-1772
HEK293T	ATCC	CTRL-3216
Experimental models: Organisms/strains		
Mouse: male and female wild-type C57BL/6J	The Jackson Laboratory	000664
Mouse: GPx4 heterogeneous KO ($GPx4^{+/-}$)	Yant et al. 2003.	
Mouse: GPx4 overexpression (GPx4Tg)	Ran et al. 2004.	
Mouse: GPx4 conditional KO (GPx4 cKO+/+)	The Jackson Laboratory	027964
Mouse: ATG3 conditional KO (ATG3 cKO+/+)	Cai et al. 2018.	
Mouse: HSA-MerCreMer +/-	McCarthy et al. 2012.	
Oligonucleotides		
Mouse GPx4 shRNA	Millipore Sigma	TRCN0000076552
Mouse LPCAT3 shRNA	Millipore Sigma	TRCN0000121437
Mouse ATG3 shRNA	Millipore Sigma	TRCN0000247442
Packaging Vector psPAX2	Addgene	12260
Envelope Vector pMD2.G	Addgene	12259
Scrambled shRNA plasmid	Addgene	1864
Mouse GPx4 Fwd Primer: GCTGAGAATTCGTGCATGG	U of U Genomics Core	
Mouse GPx4 ReV Primer: CCGTCTGAGCCGCTTACTTA	U of U Genomics Core	
Mouse ATG3 Fwd Primer: ACACGGTGAAGGGAAAGGC	U of U Genomics Core	
Mouse ATG3 Rev Primer: TGGTGGACTAAGTGATCTCCAG	U of U Genomics Core	
Mouse CHAC1 Fwd Primer: CTGTGGATTTTCGGGTACGG	U of U Genomics Core	
Mouse CHAC1 Rev Primer: CCCCTATGGAAGGTGTCTCC	U of U Genomics Core	
Mouse PTGS2 Fwd Primer: TGAGCAACTATTCCAAACCAGC	U of U Genomics Core	
Mouse PTGS2 Rev Primer: GCACGTAGTCTTCGATCACTATC	U of U Genomics Core	

Mouse LPCAT3 Fwd Primer: GGCCTCTCAATTGCTTATTTCA	U of U Genomics Core	
Mouse LPCAT3 Rev Primer: AGCACGACACATAGCAAGGA	U of U Genomics Core	
Software and algorithms		
GraphPad Prism 9.3	GraphPad	N/A
ImageJ	NIH	N/A

Animal models

GPx4+/- and GPx4Tg mice were generated previously [16, 27]. Conditional GPx4 knockout (GPx4cKO+/+) mice were acquired from Jackson Laboratory (Stock No: 027964) [18]. Conditional ATG3 knockout (ATG3cKO+/+) mice were previously described [35]. GPx4cKO+/+ mice or ATG3cKO+/+ mice were then crossed with tamoxifen-inducible, skeletal muscle–specific Cre recombinase (HSA-MerCreMer+/-) mice [36] to generate GPx4cKO+/+; HSAMerCreMer-/- (control) and GPx4cKO+/+; HSA-MerCreMer+/- (skeletal muscle–specific GPx4 knockout; GPx4-MKO) mice or ATG3cKO+/+; HSAMerCreMer-/- (control) and ATG3cKO+/+; HSA-MerCreMer+/- (ATG3-MKO) mice. Tamoxifen-injected (7.5 μg/g body mass, 5 consecutive days) littermates were used. Mice were maintained on a 12-hour light/12-hour dark cycle in a temperature-controlled room. Body composition measurements were taken immediately before terminal experiments with a Bruker Minispec MQ20 nuclear magnetic resonance (NMR) analyzer (Bruker, Rheinstetten, Germany). All mice were bred onto C57BL/6J background and were born at normal Mendelian ratios. Body mass were measured every day during HU. All protocols were approved by Institutional Animal Care and Use Committees at the University of Utah.

Hindlimb unloading

Mice underwent 1, 7, or 14 days of HU (2 mice/cage) using a previously described

346 protocol [14, 15] based on the traditional Morey-Holton design to study disuse atrophy
347 in rodents. Along with daily monitoring of body mass, food intake was monitored every
348 other day to ensure that the mice did not experience excessive weight loss due to
349 malnutrition or dehydration. Following 1, 7, or 14 days of HU, mice were fasted for 4 h
350 and given an intraperitoneal injection of 80 mg/kg ketamine and 10 mg/kg xylazine,
351 after which tissues were harvested. Extensor digitorum longus (EDL), and soleus
352 (SOL) were carefully dissected for weight measurements.
353
354 **Muscle force generation**
355 Force-generating properties of soleus and EDL muscles were measured as previously
356 described [37, 38]. Briefly, soleus/EDL muscles were sutured at each tendon, and
357 muscles were suspended at optimal length (Lo), which was determined by pulse
358 stimulation. After Lo was identified, muscles were stimulated (0.35 seconds, pulse
359 width 0.2 milliseconds) at frequencies ranging from 10 to 200 Hz. Muscle length and
360 mass were measured to quantify cross-sectional area for force normalization.
361
362 **Quantitative reverse transcription PCR**
363 Samples were homogenized in TRIzol reagent (Life Technologies) to extract total RNA.
364 One microgram RNA was reverse-transcribed using an IScript cDNA synthesis kit (Bio-
365 Rad). Reverse transcription PCR (RT-PCR) was performed with the Viia 7 Real-Time
366 PCR System (Life Technologies) using SYBR Green reagent (Life Technologies). All
367 data were normalized to ribosomal L32 gene expression and were normalized to the
368 mean of the control group. Primers were based on sequences in public databases.
369
370 **Western blot**
371 Whole muscle or cells were homogenized, and western blots were performed as

372 previously described [14]. Protein homogenates were analyzed for abundance of
373 phosphorylated 4-hydroxynonenal (4-HNE; ab48506; Abcam), GPx4 (ab125066,
374 Abcam), actin (A2066, MilliporeSigma), GAPDH (14C10, Cell Signaling Technology),
375 p62 (ab56416, Abcam), LC3B (83506, Cell Signaling Technology).
376
377 **Mass spectrometry**
378 Oxidolipidomics samples were analyzed on the SCIEX 7500 system coupled with
379 ExionLC (SCIEX, Concord, Canada) using multiple reaction monitoring (MRM)
380 analysis. Mobile phase A is composed of 93:7 acetonitrile:dichloromethane containing
381 2mM ammonium acetate and mobile phase B is composed of 50:50 acetonitrile:water
382 containing 2mM ammonium acetate. A Phenomenex Luna® NH2 3 µm particle size
383 (4.6x150mm) was used for separation and column temperature was kept at 40°C. The
384 total flow rate is 0.7 mL/min with a total run time of 17-minutes. Samples were
385 extracted using the Bligh & Dyer method. Lower layer was collected, dried down and
386 resuspended in mobile phase A.
387
388 **Cell culture**
389 C2C12 myoblasts were grown and maintained in high-glucose Dulbecco's modified
390 Eagle's medium (DMEM), with 10% fetal bovine serum (FBS), and 0.1 %
391 penicillin/streptomycin. Once 90 to 100% confluent, C2C12 cells were differentiated
392 into myotubes with low-glucose DMEM, with l-glutamine and 110 mg/L sodium
393 pyruvate; supplemented with 2% horse serum, and 0.1% penicillin-streptomycin. For
394 experiments with erastin (E7781, MilliporeSigma), Ferrostatin-1 (SML0583,
395 MilliporeSigma), and RSL3 (SML2234, MilliporeSigma), C2C12 myotubes were
396 incubated with either 10 µM erastin/10 µM Ferrostatin-1/5 µM RSL3/ or equal-volume
397 DMSO directly dissolved into medium. For experiments with L-carnosine (C9625,

MilliporeSigma), and N-acetylcarnosine (18817, Cayman), C2C12 myotubes were incubated with 10 mM of L-carnosine/N-acetylcarnosine directly dissolved into medium.

Lentivirus-mediated knockdown of GPx4/LPCAT3/ATG3

Lentivirus-mediated knockdown of experiments were performed as previously described [15, 21, 39]. Vectors were decreased using pLKO.1 lentiviral-RNAi system. Plasmids encoding short hairpin RNA (shRNA) for mouse GPx4 (shGPx4: TRCN0000076552), mouse LPCAT3 (shLPCAT3: TRCN0000121437), and mouse ATG3 (shATG3: TRCN0000247442) were obtained from MilliporeSigma. Packaging vector psPAX2 (ID 12260), envelope vector pMD2.G (ID 12259), and scrambled shRNA plasmid (SC: ID 1864) were obtained from Addgene. HEK293T cells in 10 cm dishes were transfected using 50 µL 0.1% polyethylenimine, 200 µL 0.15 M sodium chloride, and 500 µL Opti-MEM (with HEPES, 2.4 g/L sodium bicarbonate, and l-glutamine; Gibco 31985) with 2.66 µg of psPAX2, 0.75 µg of pMD2.G, and 3 µg of either scrambled or GPx4/LPCAT3/ATG3 shRNA plasmids. After 48 hours, growth medium was collected, filtered using 0.22 µm vacuum filters, and used to treat undifferentiated C2C12 cells for 48 hours. To ensure that only cells infected with shRNA vectors were viable, cells were selected with puromycin throughout differentiation.

Measurements of myotube diameter

Images of myotubes were visualized at ×20 magnification using an inverted light microscope and captured with a camera (DP74, Olympus). Myotube diameter was measured for at least 100 myotubes from 5 random fields in each group using ImageJ software. The average diameter per myotube was calculated as the mean of ten short-axis measurements taken along the length of the myotube.

424

425 **Assessment of cell death**

426 Cell death levels were examined by counting the numbers of cells with trypan blue
427 staining. The cells were trypsinized and stained with 0.2% trypan blue for 5 min.
428 Stained and non-stained cells were counted under a microscope using a
429 hemocytometer.

430

431 **Immunofluorescence**

432 C2C12 myotubes were fixed with 4% paraformaldehyde for 10 min and permeabilized
433 with 0.2% Triton X-100 for 15 min. After blocking with bovine serum albumin,
434 immunocytochemistry was performed with anti-HNE (ab48506, Abcam), anti-lysosome
435 associated membrane protein 2 (Lamp-2) (NB300-591, Novus), and Alexa Fluor-
436 conjugated secondary antibodies Alexa Fluor® 568 (ab175472, abcam), Alexa Fluor®
437 488 (ab150073, abcam), and DAPI (D1306, Invitrogen). Images were captured using a
438 63× 1.4 NA oil immersion objective on a Leica SP5 confocal system (Leica). For an
439 experiment, C2C12 myotubes incubated with erastin with or without pretreatment of
440 BaFA1 (SML1661, MilliporeSigma). Soleus muscles were embedded in optimal cutting
441 temperature (OCT) gel and sectioned at 10 μm with a cryostat (Microtome Plus). The
442 sections underwent blocking for 1 hr with M.O.M. mouse IgG Blocking Reagent (Vector
443 Laboratories, MKB-2213), 1 hr with primary antibodies (BA.D5, SC.71, BF.F3 all at
444 1:100 from DSHB). Sections were then probed with the following secondary antibodies:
445 Alexa Fluor 647 (1:250; Invitrogen, A21242), Alexa Fluor 488 (1:500; Invitrogen,
446 A21121), and Alexa Fluor 555 (1:500; Invitrogen, A21426). Negative stained fibers
447 were considered to be IIx. Slides were imaged with an automated wide-field light
448 microscope (Nikon Corp.) using a 10x objective lens. Cross-sectional area and fiber
449 type composition was then quantified utilizing ImageJ software.

Mitochondrial respiration measurements

Mitochondrial O_2 utilization was measured using the Oroboros O_2K Oxygraphs, as previously described [14, 15]. Isolated mitochondria were added to the oxygraph chambers containing buffer Z. Respiration was measured in response to the following substrate concentrations: 0.5 mM malate, 5 mM pyruvate, 2 mM ADP, 10 mM succinate, and 1.5 µM FCCP.

Mitochondrial H_2O_2 measurements

Mitochondrial H_2O_2 production was measured using the Horiba Fluoromax-4, as previously described [14, 15]. Briefly, skeletal muscle was minced in mitochondria isolation medium (300 mM sucrose, 10 mM HEPES, 1 mM EGTA) and subsequently homogenized using a Teflon glass system. Homogenates were then centrifuged at 800 g for 10 min, after which the supernatant was taken and centrifuged at 12,000 g for 10 min. The resulting pellet was carefully resuspended in mitochondria isolation medium. JH_2O_2 was measured in buffer Z (MES potassium salt; 105 mM, KCl 30 mM, KH_2PO_4 10 mM, $MgCl_2$ 5 mM, and BSA 0.5 mg/ml) supplemented with 10 µM Amplex UltraRed (Invitrogen) and 20 U/mL CuZnSOD in the presence of the following substrates: 10 mM succinate, 100 µM 1,3-bis(2-chloroethyl)-1-nitrosourea (BCNU/carmustine), and 1 µM auranofin. The appearance of the fluorescent product was measured with excitation/emission at 565/600 nm.

Administration of L-carnosine/N-acetylcarnosine in vivo.

Carnosine was administered as previously described [31]. Briefly, young (4-month-old) or old (20-month-old) C57BL/6J mice were supplemented with 80 mM carnosine dissolved in drinking water (pH 7.5) for 2 weeks (1 week of pretreatment and 1 week

476 during HU). Bottles were refreshed two times a week (L-carnosine, C9625,
477 MilliporeSigma), and or everyday (N-acetyl carnosine, 18817, Cayman).
478
479 **MDA quantification**
480 MDA content was quantified in fresh gastrocnemius muscles using a lipid peroxidation
481 assay kit (ab118970, Abcam) according to the manufacturer's instruction. Rates of
482 appearance of MDA-thiobarbituric acid adduct were quantified colorimetrically at 532
483 nm using a spectrophotometer.
484
485 **Statistical analyses**
486 Data are presented as means ± s.e.m. Statistical analyses were performed using
487 GraphPad Prism 7.03. Independent sample t-tests (two-sided) were used to compare
488 two groups. For multiple comparisons, one- or two-way analysis of variance (ANOVA)
489 were performed followed by appropriate post-hoc tests corrected for multiple
490 comparisons. For all tests $P < 0.05$ was considered statistically significant.

References

1. Evans, W.J., *Skeletal muscle loss: cachexia, sarcopenia, and inactivity.* Am J Clin Nutr, 2010. **91**(4): p. 1123S-1127S.
2. Larsson, L., et al., *Sarcopenia: Aging-Related Loss of Muscle Mass and Function.* Physiol Rev, 2019. **99**(1): p. 427-511.
3. Bonaldo, P. and M. Sandri, *Cellular and molecular mechanisms of muscle atrophy.* Dis Model Mech, 2013. **6**(1): p. 25-39.
4. Dolbow, D.R. and A.S. Gorgey, *Effects of Use and Disuse on Non-paralyzed and Paralyzed Skeletal Muscles.* Aging Dis, 2016. **7**(1): p. 68-80.
5. Powers, S.K., A.J. Smuder, and D.S. Criswell, *Mechanistic links between oxidative stress and disuse muscle atrophy.* Antioxid Redox Signal, 2011. **15**(9): p. 2519-28.
6. Scicchitano, B.M., et al., *The physiopathologic role of oxidative stress in skeletal muscle.* Mech Ageing Dev, 2018. **170**: p. 37-44.
7. Wiernicki, B., et al., *Excessive phospholipid peroxidation distinguishes ferroptosis from other cell death modes including pyroptosis.* Cell Death Dis, 2020. **11**(10): p. 922.
8. Yang, W.S., et al., *Regulation of ferroptotic cancer cell death by GPX4.* Cell, 2014. **156**(1-2): p. 317-331.
9. Bochkov, V.N., et al., *Generation and biological activities of oxidized phospholipids.* Antioxid Redox Signal, 2010. **12**(8): p. 1009-59.
10. Anderson, E.J., et al., *A carnosine analog mitigates metabolic disorders of obesity by reducing carbonyl stress.* J Clin Invest, 2018. **128**(12): p. 5280-5293.
11. Bhattacharya, A., et al., *Denervation induces cytosolic phospholipase A2-mediated fatty acid hydroperoxide generation by muscle mitochondria.* J Biol Chem, 2009. **284**(1): p. 46-55.
12. Pharaoh, G., et al., *Targeting cPLA2 derived lipid hydroperoxides as a potential intervention for sarcopenia.* Sci Rep, 2020. **10**(1): p. 13968.
13. Kagan, V.E., et al., *Oxidized arachidonic and adrenic PEs navigate cells to ferroptosis.* Nat Chem Biol, 2017. **13**(1): p. 81-90.
14. Eshima, H., et al., *Neutralizing mitochondrial ROS does not rescue muscle atrophy induced by hindlimb unloading in female mice.* J Appl Physiol (1985), 2020. **129**(1): p. 124-132.
15. Heden, T.D., et al., *Mitochondrial PE potentiates respiratory enzymes to amplify skeletal muscle aerobic capacity.* Sci Adv, 2019. **5**(9): p. eaax8352.
16. Yant, L.J., et al., *The selenoprotein GPX4 is essential for mouse development and protects from radiation and oxidative damage insults.* Free Radic Biol Med, 2003. **34**(4): p. 496-502.
17. Katunga, L.A., et al., *Obesity in a model of gpx4 haploinsufficiency uncovers a causal role for lipid-derived aldehydes in human metabolic disease and cardiomyopathy.* Mol Metab, 2015. **4**(6): p. 493-506.
18. Yoo, S.E., et al., *Gpx4 ablation in adult mice results in a lethal phenotype accompanied by neuronal loss in brain.* Free Radic Biol Med, 2012. **52**(9): p. 1820-7.
19. Imai, H. and Y. Nakagawa, *Biological significance of phospholipid hydroperoxide glutathione peroxidase (PHGPx, GPx4) in mammalian cells.* Free Radic Biol Med, 2003. **34**(2): p. 145-69.
20. Lee, J.Y., et al., *Lipid Metabolism and Ferroptosis.* Biology (Basel), 2021. **10**(3).
21. Ferrara, P.J., et al., *Lysophospholipid acylation modulates plasma membrane lipid organization and insulin sensitivity in skeletal muscle.* J Clin Invest, 2021.

131(8).
22. Ferrara, P.J., et al., *Low lysophosphatidylcholine induces skeletal muscle myopathy that is aggravated by high-fat diet feeding.* FASEB J, 2021. **35**(10): p. e21867.
23. Gao, H., et al., *Ferroptosis is a lysosomal cell death process.* Biochem Biophys Res Commun, 2018. **503**(3): p. 1550-1556.
24. Ichimura, Y., et al., *A ubiquitin-like system mediates protein lipidation.* Nature, 2000. **408**(6811): p. 488-92.
25. Chen, X., et al., *Cellular degradation systems in ferroptosis.* Cell Death Differ, 2021. **28**(4): p. 1135-1148.
26. Gao, M., et al., *Ferroptosis is an autophagic cell death process.* Cell Res, 2016. **26**(9): p. 1021-32.
27. Ran, Q., et al., *Transgenic mice overexpressing glutathione peroxidase 4 are protected against oxidative stress-induced apoptosis.* J Biol Chem, 2004. **279**(53): p. 55137-46.
28. Dixon, S.J., et al., *Ferroptosis: an iron-dependent form of nonapoptotic cell death.* Cell, 2012. **149**(5): p. 1060-72.
29. Codenotti, S., et al., *Cell growth potential drives ferroptosis susceptibility in rhabdomyosarcoma and myoblast cell lines.* J Cancer Res Clin Oncol, 2018. **144**(9): p. 1717-1730.
30. Cripps, M.J., et al., *Carnosine scavenging of glucolipotoxic free radicals enhances insulin secretion and glucose uptake.* Sci Rep, 2017. **7**(1): p. 13313.
31. Everaert, I., et al., *Gene expression of carnosine-related enzymes and transporters in skeletal muscle.* Eur J Appl Physiol, 2013. **113**(5): p. 1169-79.
32. Boldyrev, A.A., G. Aldini, and W. Derave, *Physiology and pathophysiology of carnosine.* Physiol Rev, 2013. **93**(4): p. 1803-45.
33. Brown, J.L., et al., *Lipid hydroperoxides and oxylipins are mediators of denervation induced muscle atrophy.* Redox Biol, 2022. **57**: p. 102518.
34. Delfinis, L.J., et al., *Muscle weakness precedes atrophy during cancer cachexia and is linked to muscle-specific mitochondrial stress.* JCI Insight, 2022.
35. Cai, J., et al., *Autophagy Ablation in Adipocytes Induces Insulin Resistance and Reveals Roles for Lipid Peroxide and Nrf2 Signaling in Adipose-Liver Crosstalk.* Cell Rep, 2018. **25**(7): p. 1708-1717 e5.
36. McCarthy, J.J., et al., *Inducible Cre transgenic mouse strain for skeletal muscle-specific gene targeting.* Skelet Muscle, 2012. **2**(1): p. 8.
37. Ferrara, P.J., et al., *Hypothermia Decreases O2 Cost for Ex Vivo Contraction in Mouse Skeletal Muscle.* Med Sci Sports Exerc, 2018. **50**(10): p. 2015-2023.
38. Verkerke, A.R.P., et al., *Phospholipid methylation regulates muscle metabolic rate through Ca(2+) transport efficiency.* Nat Metab, 2019. **1**(9): p. 876-885.
39. Johnson, J.M., et al., *Alternative splicing of UCP1 by non-cell-autonomous action of PEMT.* Mol Metab, 2020. **31**: p. 55-66.

Acknowledgements

This research is supported by NIH grants DK107397, DK127979, GM144613, AG074535, AG063077, (to K.F.), AG050781 (to M.J.D.), HL122863, AG057006 (E.J.A), AG064078 (to Q.R.), HL149870 (S.B.), HL139451 (to Z.S.M), DK130555 (to A.D.P.), AG073493 (to J.J.P.), American Heart Association grants 915674 (to P.S.), 18PRE33960491 (to A.R.P.V.), and 19PRE34380991 (to J.M.J.), Larry H. & Gail Miller Family Foundation (to P.J.F.), University of Utah Center on Aging Pilot Grant (to K.F.), and Uehara Memorial Foundation (to H.E.). We would like to thank Diana Lim from the University of Utah Molecular Medicine Program for assistance with figures.

Author contributions

H.E. and K.F. contributed to study concept design and wrote the manuscript. P.S. and J.L.S. contributed to study design and data analysis. M.J.P., J.A.M., and J.E.C. performed mass spectrometry analyses. M.J.D. and Z.S.M. performed human muscle biopsies. H.E., P.S., J.L.S., A.W.L., J.M.J., J.J.P., A.S., and E.R.M. performed mouse experiments. H.E. performed all biochemical assays, body composition measurements and analysis of muscle force production. A.R.P.V. and P.J.F. assisted in muscle functional measurements. P.J.F. assisted in cell culture experiments. E.J.A assisted in L-carnosine and N-acetylcarnosine experiments. S.B. and Q.R. designed and generated mouse models. All contributed to editing the manuscript.

Competing interests

No competing interests to disclose.

Materials & Correspondence

Correspondence and material requests should be addressed to K. Funai.

610 **Figure legends**

611 **Fig. 1 | LOOH increases with age in skeletal muscle. (A**,**B)** GPx4 mRNA levels in
612 skeletal muscle biopsy samples from young and old humans (*n* = 9 for young, *n* = 18
613 for old) **(A)** or skeletal muscles from young and old mice (*n* = 8 for young, *n* = 7 for old)
614 **(B)**. **(C,D)** Oxidized phospholipid content in skeletal muscle from young and old mice (*n*
615 = 8 per group). (**E**,**F**,**G)** Immunoblotting **(E)** and quantification **(F)** of 4-HNE proteins (*n*
616 = 5 per group) and MDA levels **(G)** (*n* = 3 per group). Data are shown as the mean ±
617 SEM. Statistical analyses in **(A**,**B**,**C**,**D,F)** and (**G)** were performed with an unpaired two-
618 tailed t-test.

619

620 **Fig. 2 | Elevated LOOH is sufficient to promote atrophy in cultured myotubes. (A)**
621 A schematic of how pathways that regulate LOOH may promote muscle atrophy.
622 PUFA: phospholipids containing polyunsaturated fatty acids. **(B,C)** Representative
623 images **(B)** and quantification **(C)** of myotube diameter (*n* = 104 for scrambled: SC, *n* =
624 107 for GPx4 KD, *n* = 117 for Vehicle, *n* = 120 for erastin, *n* = 104 for Vehicle, *n* = 110
625 for RSL3). Scale bar, 100 μm. **(D**) GPx4 mRNA levels in C2C12 myotubes with or
626 without GPx4 knockdown (GPx4 KD) (*n* = 6 per group). **(E,F,G)** Immunoblotting of 4-
627 HNE, GPx4, and actin **(E)**, quantification of 4-HNE **(F)** proteins and MDA levels **(G)** (*n* =
628 3 per group). **(H)** mRNA levels for CHAC1 and PTGS2, markers of ferroptosis (*n* = 6
629 per group). **(I)** cell death levels in GPx4 KD myoblast or myotubes (*n* = 3 independent
630 repeats). Data are shown as the mean ± SEM. Statistical analyses in **(C,D,F,G)** and **(I)**
631 were performed with an unpaired two-tailed t-test. Statistical analyses in **(H)** were
632 performed with a two-way ANOVA and Tukey's multiple comparison test.

633

634 **Fig. 3 | Elevated LOOH is sufficient to augment disuse-induced muscle atrophy**
635 **in young and old mice. (A)** Soleus muscle mass from young or old WT or $GPx4^{+/-}$

636 mice with or without HU (*n* = 8-11 per young group, *n* = 4-8 per old mice group). **(B)**
637 Immunoblotting of 4-HNE from old WT or GPx4$^{+/-}$ mice. **(C)** Force-frequency curve from
638 old WT or GPx4$^{+/-}$ mice (*n* = 4-7 per group). **(D)** mRNA levels of GPx4 from young
639 control or GPx4-MKO mice (*n* = 4 per group). **(E,F)** Soleus muscle mass **(E)** (*n* = 7-8
640 per group) or force-frequency curve **(F)** from young control or GPx4-MKO mice (*n* = 4-7
641 per group). **(G)** Immunoblotting of 4-HNE and GPx4 from young GPx4-MKO. **(H,I)**
642 Representative images of MHC immunofluorescence **(H)** and muscle fiber CSA by fiber
643 type **(I)** for soleus muscles in young control or GPx4-MKO mice with HU (*n* = 4 per
644 group). Scale bar, 100μm. Data are shown as the mean ± SEM. Statistical analyses in
645 **(D)** were performed with an unpaired two-tailed t-test. Statistical analyses in **(A,C,E,F)**
646 and **(I)** were performed with a two-way ANOVA and multiple comparisons were
647 performed using Tukey's **(C,E,F,I)** or Sidak's **(A)** multiple comparisons tests.
648
649 **Fig. 4 | Suppression of PUFA incorporation prevents LOOH-induced myotube**
650 **atrophy. (A)** mRNA levels of LPCAT3 in C2C12 myotubes with or without LPCAT3 KD
651 (*n* = 3 per group). **(B)** Immunoblotting of 4-HNE, GPx4 and Actin protein in C2C12
652 myotubes with or without GPx4 KD and/or LPCAT3 KD. **(C)** Quantification of 4-HNE
653 proteins in C2C12 myotubes with or without LPCAT3 KD and/or GPx4 KD (*n* = 3 per
654 group). **(D,E)** Representative images **(D)**, and quantification of myotube diameter **(E)**
655 from C2C12 myotubes with or without GPx4 KD and/or without LPCAT3 KD (*n* = 104-
656 114 per group). Scale bar, 100 μm. **(F,G)** Immunoblotting **(F)** and quantification **(G)** of
657 4-HNE from C2C12 myotubes with or without LPCAT 3 KD and/or erastin (*n* = 3 per
658 group). **(H)** Representative images from C2C12 myotubes with or without LPCAT3 KD
659 and/or erastin (*n* = 3 independent repeats). Scale bar, 100 μm. Data are shown as the
660 mean ± SEM. Statistical analyses in **(A)** were performed with an unpaired two-tailed t-
661 test. Statistical analysis in **(C)** and **(G)** were performed with a two-way ANOVA and

multiple comparisons were performed using Tukey's multiple comparisons tests. Statistical analyses in **(E)** was performed with a one-way ANOVA with Dunnett's multiple comparisons test.

Fig. 5 | Suppression of autophagy-lysosome axis prevents LOOH-induced myotube atrophy. (A,B) Representative images **(A)**, and quantification of myotube diameter **(B)** from erastin-stimulated C2C12 myotubes with proteasomal inhibitor MG132 or lysosomal inhibitor BaFA1. (*n* = 21-120 per group). Scale bar, 100 μm. **(C)** Autophagic flux analyses immunoblotting for LC3-I, LC3-II, p62, and actin in SC or GPx4 KD C2C12 myotubes with or without BafA1. **(D,E)** Representative images **(D)** and quantification of myotube diameter **(E)** from C2C12 myotubes with or without GPx4 KD and/or ATG3 KD) (*n* = 104-121 per group). Data are shown as the mean ± SEM. Statistical analyses in **(B,E)** were performed with a one-way ANOVA with Dunnett's multiple comparisons test.

Fig. 6 | Muscle-specific ATG3 deletion attenuates disuse-induced atrophy and weakness. (A) mRNA levels of ATG3 (*n* = 8-32 per group) from young control or ATG3-MKO mice. (**B)** Immunoblotting of p62, LC3, and GAPDH proteins from skeletal muscles from control and ATG3-MKO mice. **(C)** Soleus muscle mass from control or ATG3-MKO mice (*n* = 10-12 per group). **(D)** Force-frequency curve from young control or ATG3-MKO mice (*n* = 9-12 per group). **(E,F)** Representative images of MHC immunofluorescence **(E)** and muscle fiber CSA by fiber type **(F)** of soleus muscles in young control or ATG3-MKO mice with HU (*n* = 6 per group). Data are shown as the mean ± SEM. Statistical analyses in **(A)** were performed with an unpaired two-tailed t-test. Statistical analyses in **(C,D)** and **(F)** were performed with a two-way ANOVA and multiple comparisons were performed using Tukey's multiple comparisons tests.

688

689 **Fig. 7 | Inhibition of autophagy-lysosome axis prevents accumulation of LOOH.**
690 **(A,B)** Immunoblotting **(A)** and quantification **(B)** of 4-HNE, GPx4, and actin in C2C12
691 myotubes with or without GPx4 KD and/or ATG3 KD. **(C,D)** Immunoblotting **(C)** and
692 quantification **(D)** of 4-HNE protein from C2C12 myotubes with or without erastin and/or
693 BaFA1 (*n* = 3 per group). **(E)** Confocal fluorescence microscope images of erastin-
694 stimulated myotubes with or without BaFA1. Scale bar, 10μm. Boxed regions are
695 shown enlarged at far right. Scale bar, 2.5 μm. **(F,G,H)** Representative images (**F**),
696 immunoblotting of 4-HNE and actin (**G**), and quantification (**H**) of H_2O_2 or BCNU-
697 stimulated C2C12 myotubes with or without BaFA1. Scale bar, 100 μm. Data are
698 shown as the mean ± SEM. Statistical analyses in **(B,D)** and **(H)** were performed with a
699 two-way ANOVA and Tukey's multiple comparison test.

700

701 **Fig. 8 | Overexpression of GPx4 ameliorates disuse-induced muscle atrophy and**
702 **weakness in young and old mice. (A)** Soleus muscle mass from young or old WT or
703 GPx4Tg mice with or without HU (*n* = 6-11 per young group, *n* = 7 per old group). **(B)**
704 Force-frequency curve from old WT or GPx4Tg mice (*n* = 5-7 per group). **(C)**
705 Immunoblotting of muscle 4-HNE from old WT or GPx4Tg mice. **(D,E)** Representative
706 images of MHC immunofluorescence **(D)** and muscle fiber CSA by fiber type **(E)** for
707 soleus muscles in old WT or GPx4Tg mice with HU (*n* = 4-6 per group). **(F)**
708 Immunoblotting of 4-HNE, and actin in C2C12 myotubes with or without GPx4 KD
709 and/or Ferrostatin-1. **(G,H)** Representative images **(G)**, and quantification of myotube
710 diameter **(H)** from C2C12 myotubes with GPx4 KD and/or Ferrostatin-1 treatments (*n* =
711 102-110 per group). Scale bar, 100 μm. Data are shown as the mean ± SEM.
712 Statistical analyses in **(H)** was performed with a one-way ANOVA with Dunnett's
713 multiple comparisons test, and statistical analyses in **(A,B)** and **(E)** were performed

with a two-way ANOVA and were performed using Tukey's **(B,E)** or Sidak's **(A)** multiple comparisons tests.

Fig. 9 | Pharmacologic suppression of carbonyl stress ameliorates muscle atrophy and weakness in young and old mice. (A) Schematic illustration of the protocol for administration of N-acetylcarnosine in vivo. **(B)** Immunoblotting of muscle 4-HNE from N-acetylcarnosine treatment in old mice. **(C)** Soleus muscle mass from young or old mice with or without N-acetylcarnosine treatment (*n* = 6-8 per young group, *n* = 7 per old group). **(D)** Force-frequency curve from N-acetylcarnosine study in old mice (*n* = 4-5 per group). **(E,F)** Representative images of MHC immunofluorescence **(E)** and muscle fiber CSA by fiber type **(F)** for soleus muscles (*n* = 3-4 per group) in old mice from the N-acetylcarnosine study. Data are shown as the mean ± SEM. Statistical analyses in **(C,D)** and **(F)** were performed with a two-way ANOVA and were performed using Tukey's **(C,F)** or Sidak's **(D)** multiple comparisons tests.

729 **Supplemental Figures**

730 **Supplemental Fig. S1 | Disuse promotes LOOH in skeletal muscle. (A,B,C)** Body
731 mass **(A)**, body composition **(B)**, food intake **(C)**, following 1, and 7-days of HU from
732 young WT C57BL/6J mice (*n* = 4 for sham, *n* = 6 for 1-day HU, *n* = 6 for 7-days HU).
733 **(D,E)** Soleus muscle mass **(D)**, force-frequency curve **(E)** in soleus muscle following 1-
734 and 7-days of HU from young WT C57BL/6J mice (*n* = 4 for sham, *n* = 6 for 1-day HU,
735 *n* = 6 for 7-days HU). **(F,G)** Immunoblotting **(F)**, and quantification **(G)** of 4-HNE
736 following 1-day and 7-days of HU (*n* = 3 per group). **(H)** Rates of oxygen consumption
737 measured in isolated skeletal muscle mitochondria with Krebs cycle substrates (*n* = 4
738 for sham, *n* = 5 for 1-day HU, *n* = 5 for 7-days HU). ADP, adenosine diphosphate;
739 FCCP, carbonyl cyanide-p-trifluoromethoxyphenylhydrazone; Mal, malate; Pyr,
740 pyruvate. **(I)** Rate of mitochondrial H_2O_2 production in response to succinate or
741 Aurorafin/BCNU (*n* = 4 for sham, *n* = 5 for 1-day HU, *n* = 5 for 7-day HU). BCNU, 1,3-
742 bis[2-chloroethyl]-1-nitrosourea. **(J)** Percentage of electron leak in muscle mitochondria
743 (*n* = 4 for sham, *n* = 5 for 1-day HU, *n* = 5 for 7-days HU). Data are shown as the mean
744 ± SEM. Statistical analyses in **(A,B,C,D,G)** and **(J)** were performed with a one-way
745 ANOVA and Dunnett's multiple comparisons tests. Statistical analyses in **(E,H)** and **(I)**
746 were performed with a two-way ANOVA and Tukey's multiple comparison test.
747
748 **Supplemental Fig. S2 | Elevated LOOH is sufficient to promote atrophy in**
749 **cultured myotubes. (A,B,C,D,E)** Quantification of 4-HNE **(A)**, immunoblotting of 4-
750 HNE **(B)** proteins, MDA levels **(C)**, mRNA levels for CHAC1 and PTGS2, markers of
751 ferroptosis **(D)**, and cell death levels **(E)** in erastin-stimulated C2C12 myotubes (*n* = 3
752 independent repeats). **(F,G,H,I)** mRNA levels of GPx4 **(F)**, immunoblotting of GPx4 and
753 actin **(G)**, quantification of GPx4 **(H)**, CHAC1 and PTGS2, markers of ferroptosis (**I**) in
754 RSL3-stimulated C2C12 myotubes (*n* = 6 per group). Data are shown as the mean ±

SEM. Statistical analyses in **(C,D,E,F,H,I)** and were performed with an unpaired two-tailed t-test. Statistical analyses in **(A)** were performed with a one-way ANOVA and Dunnett's multiple comparisons tests.

Supplemental Fig. S3 | Additional data from GPx4$^{+/-}$ mice. (A) Body mass from young and old WT or GPx4$^{+/-}$ mice. **(B,C)** body composition from young (n = 9 for WT sham, n = 8 for GPx4$^{+/-}$ sham, n = 7 for WT HU, n = 6 for GPx4$^{+/-}$ HU) **(B)** and old (n = 4 for WT sham, n = 5 for GPx4$^{+/-}$ sham, n = 8 for WT HU, n = 6 for GPx4$^{+/-}$ HU) (**C**) WT or GPx4$^{+/-}$ mice. **(D)** Food intake during hindlimb unloading (HU) in young (n = 7 for WT, n = 6 for GPx4$^{+/-}$) and old (n = 8 for WT, n = 6 for GPx4$^{+/-}$) WT or GPx4$^{+/-}$ mice. **(E)** EDL muscle mass from young (n = 9 for WT sham, n = 8 for GPx4$^{+/-}$ sham, n = 7 for WT HU, n = 6 for GPx4$^{+/-}$ HU) and old (n = 9 for WT sham, n = 8 for GPx4$^{+/-}$ sham, n = 7 for WT HU, n = 6 for GPx4$^{+/-}$ HU) WT or GPx4$^{+/-}$ mice. **(F)** Quantification of muscle 4-HNE from old mice (n = 3 per group). **(G)** MDA levels from old mice (n = 3 per group). (**H**) Force-frequency curve from soleus muscle from young WT or GPx4$^{+/-}$ mice (n = 5 for WT sham, n = 5 for GPx4$^{+/-}$ sham, n = 7 for WT HU, n = 5 for GPx4$^{+/-}$ HU). **(I,J)** Force-frequency curve in EDL muscle from young (n = 5 for WT sham, n = 5 for GPx4$^{+/-}$ sham, n = 7 for WT HU, n = 5 for GPx4$^{+/-}$ HU) **(I)** and old (n = 3 for WT sham, n = 4 for GPx4$^{+/-}$ sham, n = 6 for WT HU, n = 6 for GPx4$^{+/-}$ HU) **(J)** WT or GPx4$^{+/-}$ mice. Data are shown as the mean ± SEM. Statistical analyses in **(A,B,C,D,E,F,G,H,I,J)** were performed with a two-way ANOVA and using Tukey's multiple comparisons tests.

Supplemental Fig. S4 | Additional data from GPx4-MKO mice. (A) Genotyping gel for GPx4cKO+/+ mice crossed with HSA-MerCreMer+/- mice to yield GPx4cKO+/+; HSA-MerCreMer+/- (GPx4-MKO) mice. Control littermates (GPx4cKO+/+; HSA-MerCreMer-/-) were used for experiments. **(B,C)** Body mass **(B)**, and body composition

781 **(C)** (*n* = 7 for Ctrl sham, *n* = 4 for GPx4-MKO sham, *n* = 7 for Ctrl HU, *n* = 8 for GPx4-
782 MKO HU). **(D)** Food intake during HU (*n* = 7 for Ctrl, *n* = 8 for GPx4-MKO). **(E,F)** EDL
783 muscle mass (*n* = 6 for Ctrl sham, *n* = 4 for GPx4-MKO sham, *n* = 7 for Ctrl HU, *n* = 8
784 for GPx4-MKO HU) **(E)** and force-frequency curve from young mice (*n* = 6 for Ctrl
785 sham, *n* = 4 for GPx4-MKO sham, *n* = 6 for Ctrl HU, *n* = 7 for GPx4-MKO HU) **(F)**. **(G)**
786 Quantification of western blotting for 4-HNE from young mice (*n* = 3 per group). **(H)**
787 mRNA levels of CHAC1 and PTGS2 in skeletal muscles (*n* = 4 per group). **(I,J)** Mean
788 muscle fiber CSA (**i**) and fiber type composition **(J)** for soleus muscles following HU (*n*
789 = 4 per group). Data are shown as the mean ± SEM. Statistical analyses in **(D)** and **(I)**
790 were performed with an unpaired two-tailed t-test. Statistical analyses in **(B,C,E,F,G,H)**
791 and **(J)** were performed with a two-way ANOVA and Tukey's multiple comparison test.
792
793 **Supplemental Fig. S5 | Additional data from LPCAT3KD. (A)** mRNA levels of GPx4
794 and LPCAT3 in C2C12 myotubes with or without GPx4 and LPCAT3 double KD (*n* = 3
795 per group). **(B)** mRNA levels of LPCAT3 from erastin-stimulated myotubes (*n* = 3 per
796 group). **(C)** Cell death levels from C2C12 myotubes with or without LPCAT3 KD and/or
797 erastin (*n* = 3 independent repeats). Data are shown as the mean ± SEM. Statistical
798 analyses in **(A)** and **(B)** were performed with an unpaired two-tailed t-test. Statistical
799 analyses in **(C)** were performed with a two-way ANOVA and Tukey's multiple
800 comparison test.
801
802 **Supplemental Fig. S6 | Autophagy-lysosome axis in LOOH-induced myotube**
803 **atrophy. (A)** Cell death levels in erastin-stimulated myotubes with MG132 or BaFA1 (*n*
804 = 3 independent repeats). **(B,C)** Representative images **(B)** and cell death level **(C)** in
805 RSL3-stimulated myotubes with BaFA1 (*n* = 3 independent repeats). **(D,E)**
806 Immunoblotting **(D)** and quantification **(E)** of LC3-I, LC3-II, p62 (all static

807 measurements without BafA1), and actin protein from C2C12 myotubes with or without
808 GPX4 KD (*n* = 4 per group). **(F,G,H)** quantification of western blotting for LC3-I **(F)**,
809 LC3-II **(G)**, and p62 **(H)** protein from GPx4 KD myotubes with or without BaFA1 (*n* = 3
810 per group). **(I)** mRNA levels of ATG3 in C2C12 myotubes with or without (*n* = 3 per
811 group). **(J)** mRNA levels of GPx4 and ATG3 from C2C12 myotubes with double
812 knockdown for ATG3 and GPx4 (*n* = 3 per group). **(K,L)** Immunoblotting **(K)** and
813 quantification **(L)** of LC3, p62, and GPx4 protein from C2C12 myotubes with or without
814 ATG3 KD (*n* = 3 per group). Data are shown as the mean ± SEM. Statistical analyses
815 in **(C,I)** and **(L)** were performed with an unpaired two-tailed t-test. Statistical analyses in
816 **(A)** were performed with a one-way ANOVA and Tukey's multiple comparison test.
817 Statistical analyses in **(E,F,G,H,I)**, and **(J)** were performed with a two-way ANOVA and
818 Tukey's multiple comparison test.
819
820 **Supplemental Fig. S7 | Additional data from ATG3-MKO mice. (A**) Genotyping of
821 ATG3cKO+/+ mice crossed with HSA-MerCreMer+/- mice to yield ATG3cKO+/+; HSA-
822 MerCreMer+/- (ATG3-MKO) mice. Control littermates (ATG3cKO+/+; HSA-MerCreMer-
823 /-) were used for experiments. **(B)** Quantification of LC3-II/I ratio in muscles from
824 control and ATG3-MKO mice (*n* = 8 per group). **(C,D,E)** Body weight **(C)**, lean mass
825 **(D)**, and fat mass **(E)** from control and ATG3-MKO mice (control sham *n* = 9, ATG3-
826 MKO sham *n* = 10, control HU *n* = 10, ATG3-MKO HU *n* = 10). (**F**) EDL muscle mass
827 (control sham *n* = 10, ATG3-MKO sham *n* = 12, control HU *n* = 10, ATG3-MKO HU *n* =
828 10). (**G**) Force frequency curve for EDL muscle (control sham *n* = 9, ATG3-MKO sham
829 *n* = 8, control HU *n* = 10, ATG3-MKO HU *n* = 9). (**H**) Fiber type composition for SOL
830 muscle (control HU *n* = 6, ATG3MKO HU *n* = 6). Data are shown as the mean ± SEM.
831 Statistical analyses in **(B,C,D,E,F,G)** and **(H)** were performed with a two-way ANOVA
832 and Tukey's multiple comparison test.

Supplemental Fig. S8 | Inhibition of autophagy-lysosome axis prevents accumulation of LOOH. (A,B) Immunoblotting **(A)** and quantification **(B)** of 4-HNE protein from C2C12 myotubes with or without erastin and/or ATG3 KD (*n* = 3 per group). **(C,D)** Immunoblotting **(C)** and quantification **(D)** of 4-HNE protein from C2C12 myotubes with or without erastin and/or BaFA1 (*n* = 3 per group). **(E)** Confocal immunofluorescence of LAMP2 (lysosome) and 4-HNE in erastin-stimulated C2C12 myotubes with or without BaFA1. Scale bar, 10μm. **(F,G)** Immunoblotting **(F)** and quantification **(G)** of 4-HNE protein from BCNU-stimulated C2C12 myotubes with or without BafA1. **(H)** A novel role of lysosome in amplifying LOOH. Data are shown as the mean ± SEM. Statistical analyses in **(B,D)** and **(G)** were performed with a two-way ANOVA and Tukey's multiple comparison test.

Supplemental Fig. S9 | Additional data from GPx4Tg mice. (A) Quantification of GPx4 proteins from WT or GPx4Tg with or without HU (*n* = 3 per group). **(B)** Body mass from young (*n* = 9 for WT, *n* = 8 for GPx4Tg) and old (*n* = 7 for WT, *n* = 7 for GPx4Tg) mice. **(C,D)** body composition from young mice **(C)** and old mice **(D)**. **(E)** Food intake during HU from young and old mice. **(F,G)** EDL muscle mass from young (*n* = 6 for WT sham, *n* = 8 for GPx4Tg sham, *n* = 9 for WT HU, *n* = 8 for GPx4Tg HU) **(F)** and old (*n* = 7 per group) **(G)** mice. **(H)** Force-frequency curve in soleus muscle from young mice (*n* = 5 for WT sham, *n* = 6 for GPx4Tg sham, *n* = 9 for WT HU, *n* = 8 for GPx4Tg HU). **(I,J)** Force-frequency curve in EDL muscle from young mice (*n* = 5 for WT sham, *n* = 7 for GPx4Tg sham, *n* = 9 for WT HU, *n* = 8 for GPx4Tg HU) **(I)** and old (*n* = 5 for WT sham, *n* = 5 for GPx4Tg sham, *n* = 5 for WT HU, *n* = 6 for GPx4Tg HU) **(J)** mice. **(K)** Quantification of muscle 4-HNE proteins from old mice (*n* = 3 per group). **(L,M)** Mean muscle fiber CSA **(L)** and fiber type composition **(M)** for soleus muscles

from old mice following HU (*n* = 6 for WT, *n* = 4 for GPx4Tg). Data are shown as the mean ± SEM. Statistical analyses in **(L)** were performed with an unpaired two-tailed t-test. Statistical analyses in **(A-M)** were performed with a two-way ANOVA and Tukey's multiple comparison test.

Supplemental Fig. S10 | Effects of ferrostatin-1 or L-carnosine treatment in vitro. **(A,B,C)** Quantification of 4-HNE proteins (*n* = 2 per group) **(A)**, cell death level (*n* = 3 independent repeats) **(B)**, and mRNA levels of CHAC1 and PTGS2 with or without GPx4 KD and/or Ferrostatin-1 (*n* = 6 for SC, *n* = 5 for GPx4 KD) **(C)** in C2C12 myotubes. **(D,E,F)** Immunoblotting **(D)** and quantification **(E)** of 4-HNE, and actin (*n* = 3 per group) and cell death level (*n* = 3 independent repeats) **(F)** with or without erastin and/or L-carnosine in C2C12 myotubes. **(G,H,I)** Immunoblotting **(G)** and quantification **(H)** of 4-HNE, and actin (*n* = 3 per group), and **(I)** cell death level (*n* = 3 independent repeats) in C2C12 myotubes with or without GPx4 KD and/or L-carnosine. Data are shown as the mean ± SEM. Statistical analyses in **(E)**, and **(F)** were performed with a one-way ANOVA and Tukey's multiple comparison test. Statistical analyses in **(A,B,C,H)** and **(I)** were performed with a two-way ANOVA and Tukey's multiple comparison test.

Supplemental Fig. S11 | L-carnosine treatment partly ameliorates disuse-induced muscle atrophy. (A,B,C,D,E,F,G) Body mass **(A)**, body composition (*n* = 6 for vehicle sham, *n* = 7 for L-carnosine sham, *n* = 12 for vehicle HU, *n* = 13 for L-carnosine HU) **(B)**, food intake **(C)**, water intake (*n* = 6 for vehicle sham, *n* = 6 for L-carnosine sham, *n* = 6 for vehicle HU, *n* = 7 for L-carnosine HU) (**D**), immunoblotting **(E)** and quantification **(F)** of 4-HNE (*n* = 3 per group), and soleus muscle mass (*n* = 6 for vehicle sham, *n* = 7 for L-carnosine sham, *n* = 12 for vehicle HU, *n* = 13 for L-carnosine HU) **(G)**. Data are

885 shown as the mean ± SEM. Statistical analyses in **(A,B,C,D,F)** and **(G)** were performed
886 with a two-way ANOVA and Tukey's multiple comparison test.
887
888 **Supplemental Fig. S12 | Effects of N-acetylcarnosine treatment in vitro. (A,B,C)**
889 Immunoblotting **(A)** and quantification **(B)** for 4-HNE, GPx4 and actin (*n* = 3 per group)
890 and cell death level (*n* = 3 independent repeats) **(C)** from C2C12 myotubes with or
891 without GPx4 KD and/or N-acetylcarnosine. **(D,E,F)** Immunoblotting **(D)** and
892 quantification **(E)** of 4-HNE and actin (*n* = 3 per group) and cell death level (*n* = 3
893 independent repeats) **(F)** in C2C12 myotubes with or without erastin and/or N-
894 acetylcarnosine. Data are shown as the mean ± SEM. Statistical analyses in **(B)** and
895 **(C)** were performed with a two-way ANOVA and Tukey's multiple comparison test.
896 Statistical analyses in **(E)** and **(F)** were performed with a one-way ANOVA and Tukey's
897 multiple comparison test.
898
899 **Supplemental Fig. S13 | Additional data from N-acetylcarnosine treatment in**
900 **vivo. (A,B,C)** Body mass **(A)**, body composition from young mice **(B)** and old mice **(C)**.
901 **(D,E,F,G)** Food intake **(D)**, water intake **(E)**, immunoblotting **(F)** and quantification **(G)**
902 of 4-HNE (*n* = 3 per group). **(H)** EDL muscle mass from young mice and old mice. **(I)**
903 Force-frequency curve in soleus muscle from young mice (*n* = 5 for vehicle sham, *n* = 6
904 for N-acetylcarnosine sham, *n* = 5 for vehicle HU, *n* = 5 for N-acetylcarnosine HU).
905 **(J,K)** Force-frequency curve in EDL muscle from young mice (*n* = 7 for vehicle sham, *n*
906 = 7 for N-acetylcarnosine sham, *n* = 6 for vehicle HU, *n* = 7 for N-acetylcarnosine HU)
907 **(J)** and old mice (*n* = 6 for vehicle sham, *n* = 7 for N-acetylcarnosine sham, *n* = 6 for
908 vehicle HU, *n* = 6 for N-acetylcarnosine HU) **(K)**. **(L,M)** Average of muscle fiber CSA (**I**)
909 and fiber type composition **(M)** for soleus muscles from old mice following HU (*n* = 3 for
910 vehicle, *n* = 4 for N-acetylcarnosine). Data are shown as the mean ± SEM. Statistical

911 analyses in **(L)** were performed with an unpaired two-tailed t-test. Statistical analyses in

912 **(A,B,C,D,E,G,H,I,J,K)** and **(M)** were performed with a two-way ANOVA and Tukey's

913 multiple comparison test.

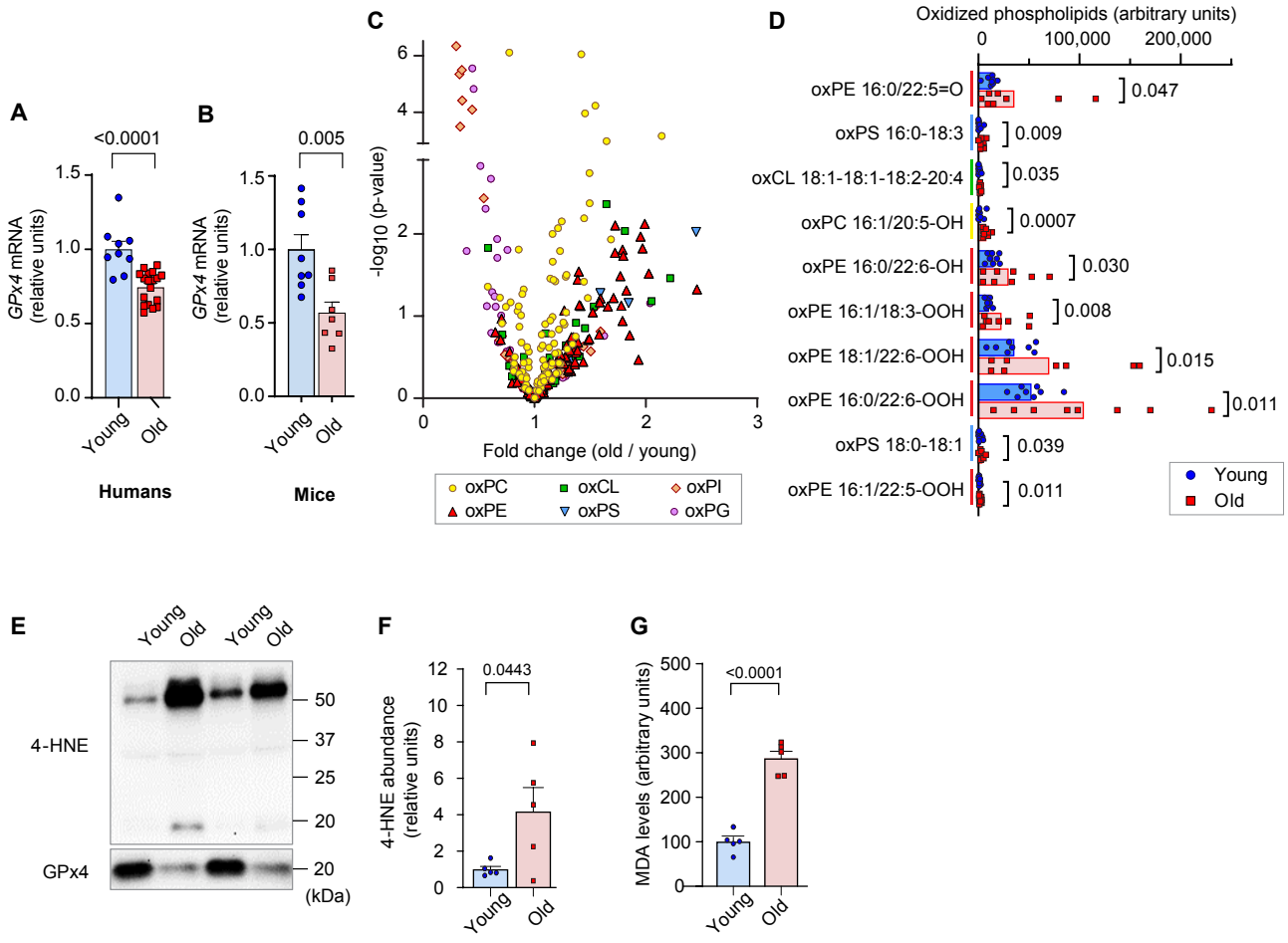
A
<0.0001
GPx4 mRNA (relative units)
Young
Old
Humans
B
0.005
Mice
C
-log10 (p-value)
Fold change (old / young)
oxPC
oxCL
oxPI
oxPE
oxPS
oxPG
D
Oxidized phospholipids (arbitrary units)
oxPE 16:0/22:5=O
0.047
oxPS 16:0-18:3
0.009
oxCL 18:1-18:1-18:2-20:4
0.035
oxPC 16:1/20:5-OH
0.0007
oxPE 16:0/22:6-OH
0.030
oxPE 16:1/18:3-OOH
0.008
oxPE 18:1/22:6-OOH
0.015
oxPE 16:0/22:6-OOH
0.011
oxPS 18:0-18:1
0.039
oxPE 16:1/22:5-OOH
0.011
Young
Old
E
4-HNE
GPx4
(kDa)
F
0.0443
4-HNE abundance (relative units)
G
<0.0001
MDA levels (arbitrary units)

Figure 1

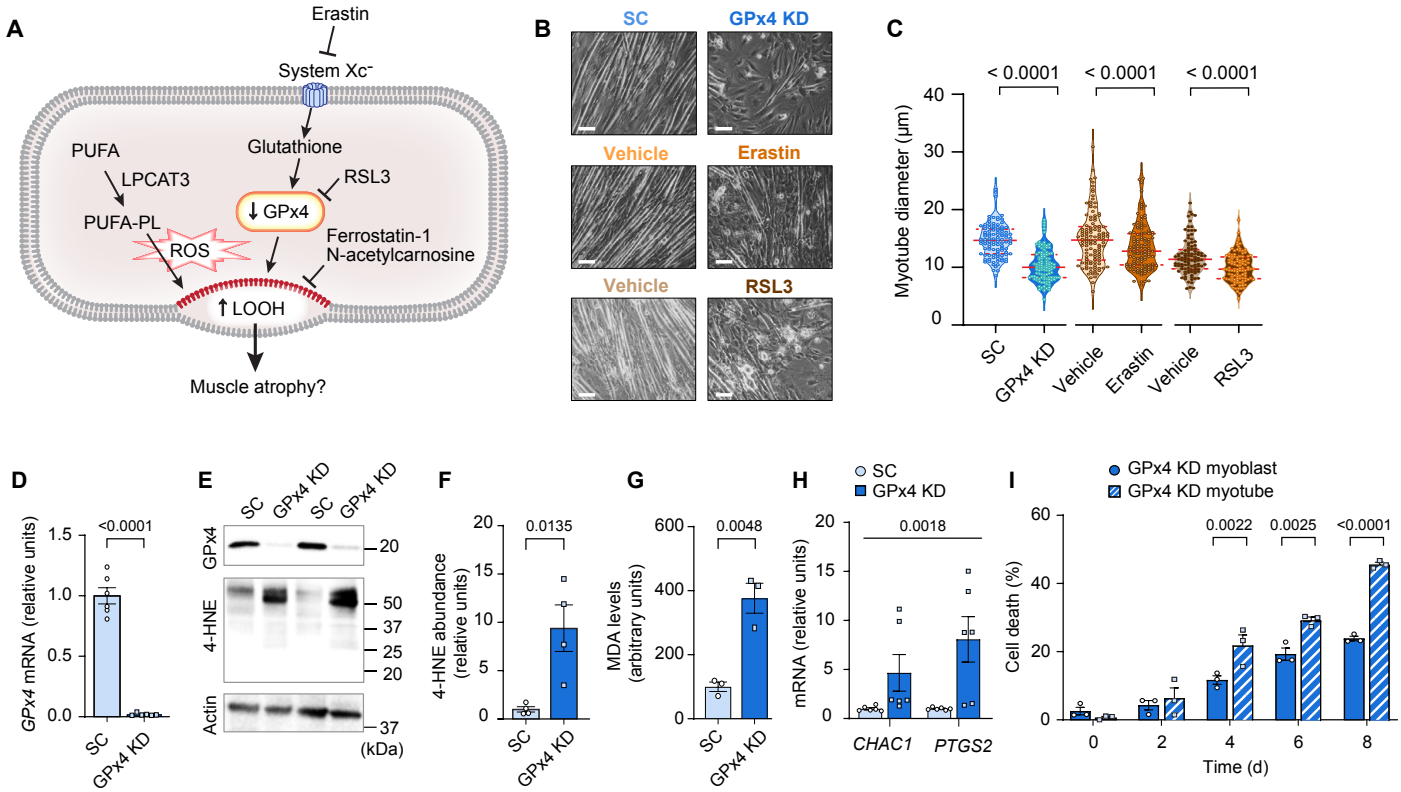
A
Erastin
System Xc-
Glutathione
PUFA
LPCAT3
RSL3
↓ GPx4
PUFA-PL
ROS
Ferrostatin-1
N-acetylcarnosine
↑ LOOH
Muscle atrophy?
B
SC
GPx4 KD
Vehicle
Erastin
Vehicle
RSL3
C
< 0.0001
< 0.0001
< 0.0001
Myotube diameter (µm)
SC
GPx4 KD
Vehicle
Erastin
Vehicle
RSL3
D
<0.0001
GPx4 mRNA (relative units)
SC
GPx4 KD
E
SC
GPx4 KD
SC
GPx4 KD
GPx4
4-HNE
Actin
(kDa)
F
0.0135
4-HNE abundance (relative units)
SC
GPx4 KD
G
0.0048
MDA levels (arbitrary units)
SC
GPx4 KD
H
SC
GPx4 KD
0.0018
mRNA (relative units)
CHAC1
PTGS2
I
GPx4 KD myoblast
GPx4 KD myotube
0.0022
0.0025
<0.0001
Cell death (%)
Time (d)

Figure 2

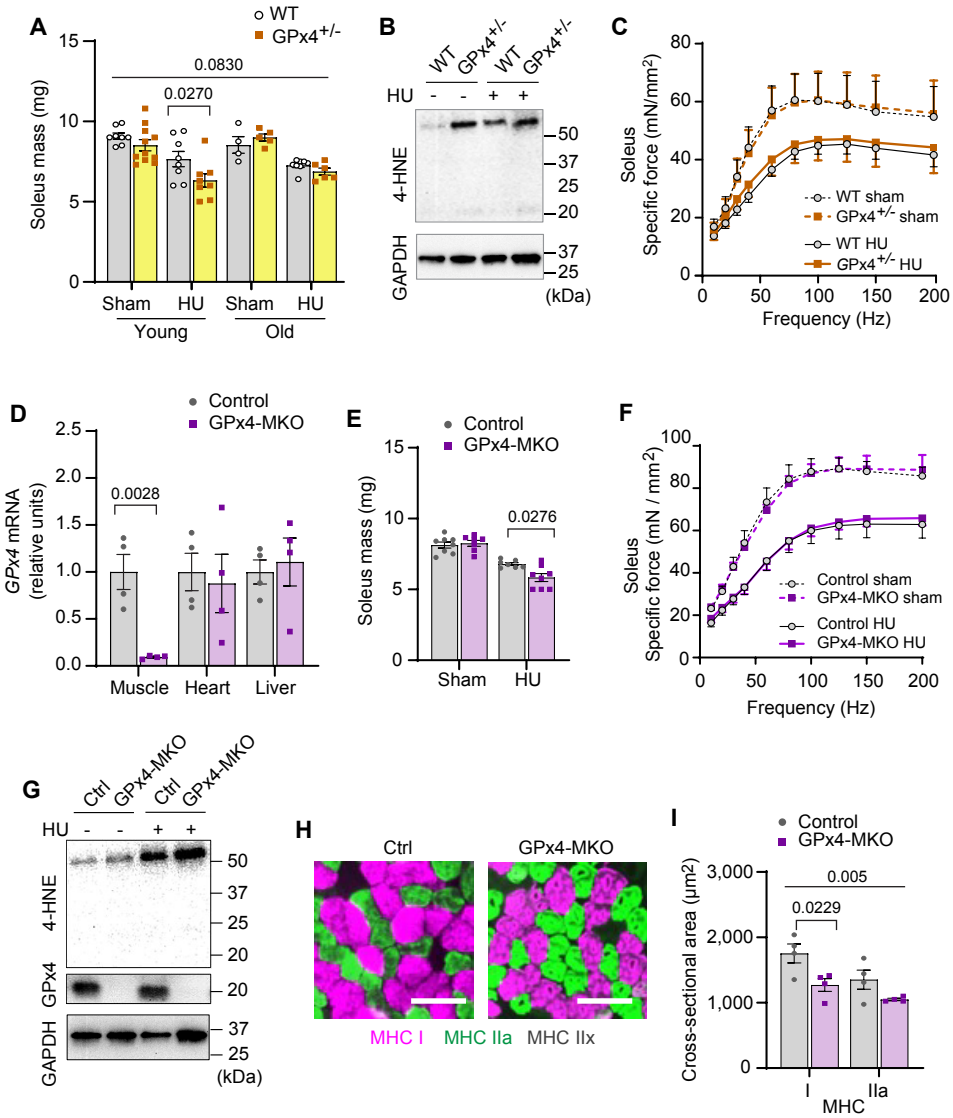
A
WT
GPx4+/-
Soleus mass (mg)
0.0830
0.0270
Sham
HU
Sham
HU
Young
Old
B
WT
GPx4+/-
WT
GPx4+/-
HU
4-HNE
GAPDH
(kDa)
C
Soleus
Specific force (mN/mm2)
WT sham
GPx4+/- sham
WT HU
GPx4+/- HU
Frequency (Hz)
D
Control
GPx4-MKO
GPx4 mRNA
(relative units)
0.0028
Muscle
Heart
Liver
E
Control
GPx4-MKO
Soleus mass (mg)
0.0276
Sham
HU
F
Soleus
Specific force (mN / mm2)
Control sham
GPx4-MKO sham
Control HU
GPx4-MKO HU
Frequency (Hz)
G
Ctrl
GPx4-MKO
Ctrl
GPx4-MKO
HU
4-HNE
GPx4
GAPDH
(kDa)
H
Ctrl
GPx4-MKO
MHC I
MHC IIa
MHC IIx
I
Control
GPx4-MKO
Cross-sectional area (µm2)
0.005
0.0229
MHC

Figure 3

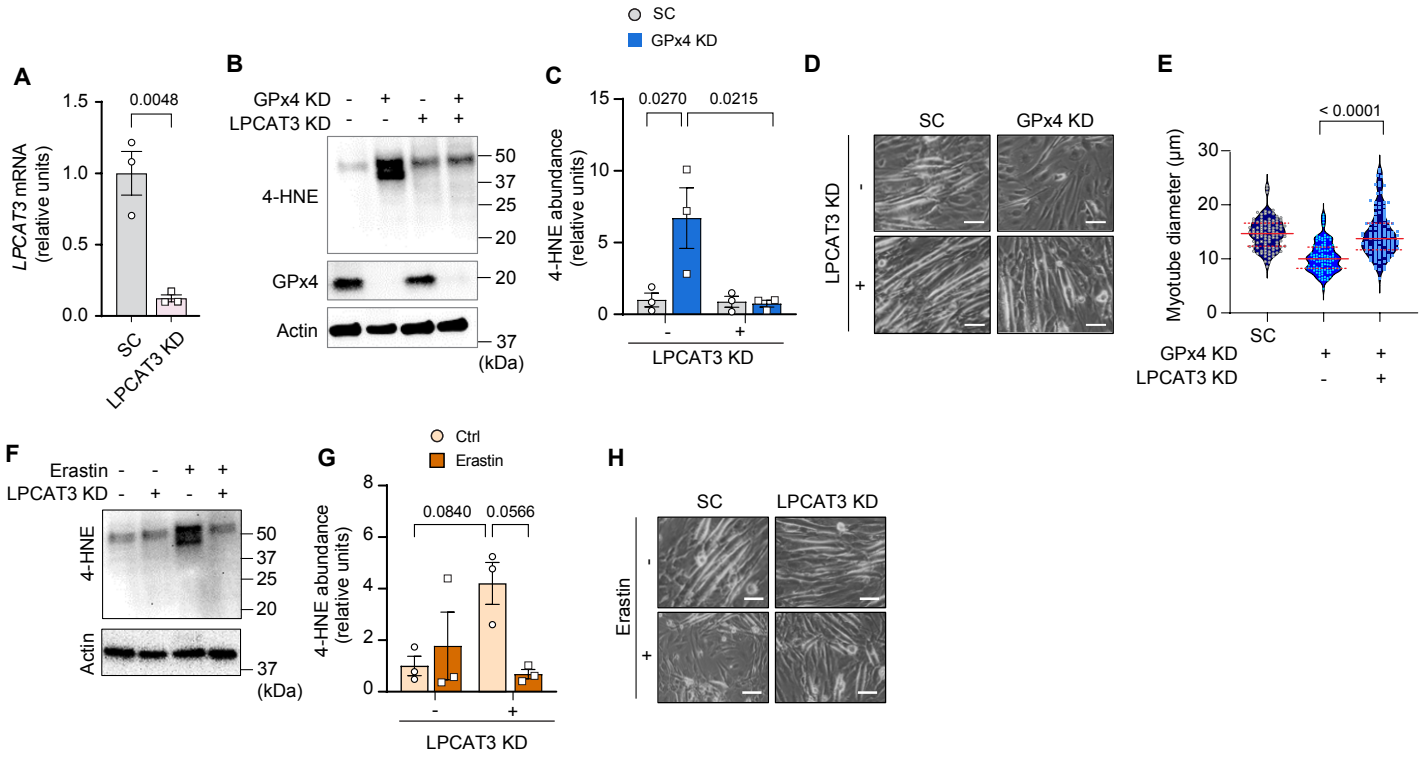
A
LPCAT3 mRNA (relative units)
1.5
1.0
0.5
0.0
0.0048
SC
LPCAT3 KD
B
GPx4 KD - + - +
LPCAT3 KD - - + +
4-HNE
GPx4
Actin
50
37
25
20
20
37
(kDa)
C
SC
GPx4 KD
4-HNE abundance (relative units)
15
10
5
0
0.0270
0.0215
-
+
LPCAT3 KD
D
SC
GPx4 KD
LPCAT3 KD
-
+
E
Myotube diameter (µm)
30
20
10
0
< 0.0001
SC
GPx4 KD + +
LPCAT3 KD - +
F
Erastin - - + +
LPCAT3 KD - + - +
4-HNE
Actin
50
37
25
20
37
(kDa)
G
Ctrl
Erastin
4-HNE abundance (relative units)
8
6
4
2
0
0.0840
0.0566
-
+
LPCAT3 KD
H
SC
LPCAT3 KD
Erastin
-
+

Figure 4

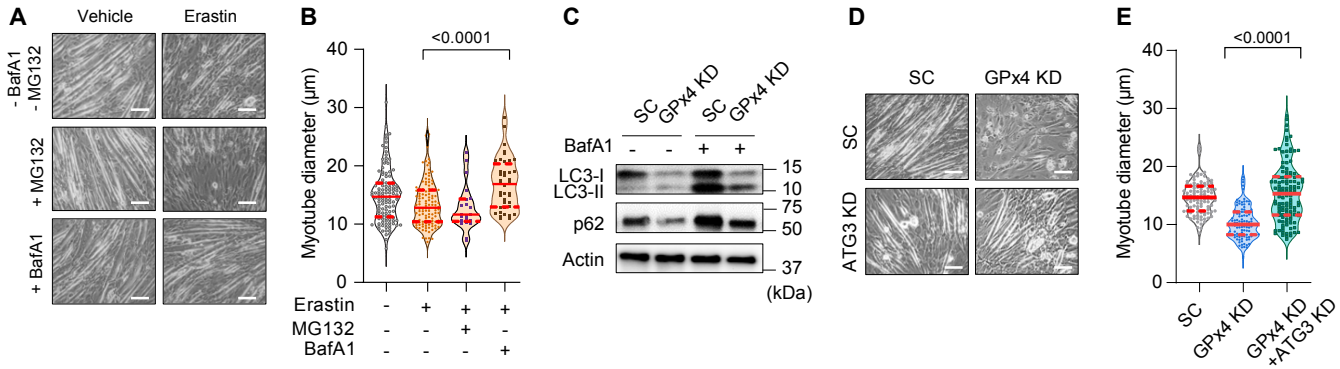
A
Vehicle
Erastin
- BafA1
- MG132
+ MG132
+ BafA1
B
<0.0001
Myotube diameter (μm)
40
30
20
10
0
Erastin - + + +
MG132 - - + -
BafA1 - - - +
C
SC
GPx4 KD
SC
GPx4 KD
BafA1 - - + +
LC3-I
LC3-II
p62
Actin
15
10
75
50
37
(kDa)
D
SC
GPx4 KD
SC
ATG3 KD
E
<0.0001
Myotube diameter (μm)
40
30
20
10
0
SC
GPx4 KD
GPx4 KD +ATG3 KD

Figure 5

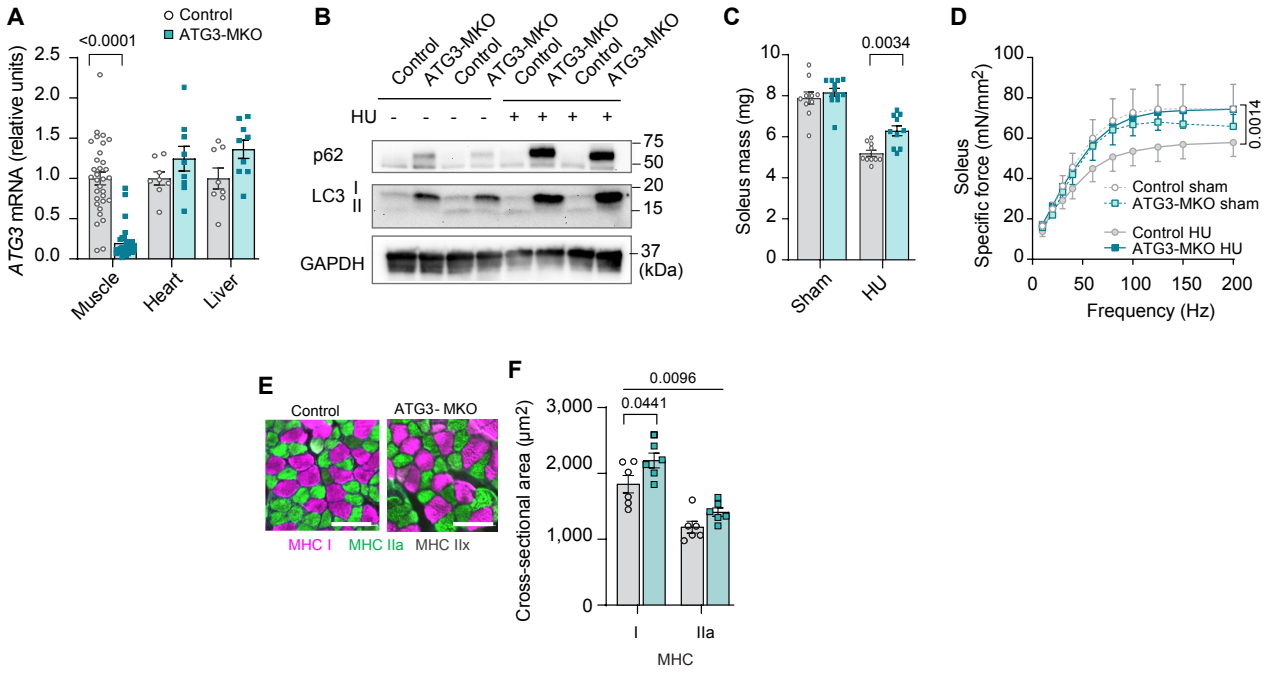
A
Control
ATG3-MKO
<0.0001
ATG3 mRNA (relative units)
2.5
2.0
1.5
1.0
0.5
0.0
Muscle
Heart
Liver
B
Control
ATG3-MKO
Control
ATG3-MKO
Control
ATG3-MKO
Control
ATG3-MKO
HU - - - - + + + +
p62
LC3 I
II
GAPDH
75
50
20
15
37
(kDa)
C
0.0034
Soleus mass (mg)
10
8
6
4
2
0
Sham
HU
D
Soleus
Specific force (mN/mm2)
100
80
60
40
20
0
0.0014
Control sham
ATG3-MKO sham
Control HU
ATG3-MKO HU
0
50
100
150
200
Frequency (Hz)
E
Control
ATG3- MKO
MHC I
MHC IIa
MHC IIx
F
0.0096
0.0441
Cross-sectional area (μm2)
3,000
2,000
1,000
0
I
IIa
MHC

Figure 6

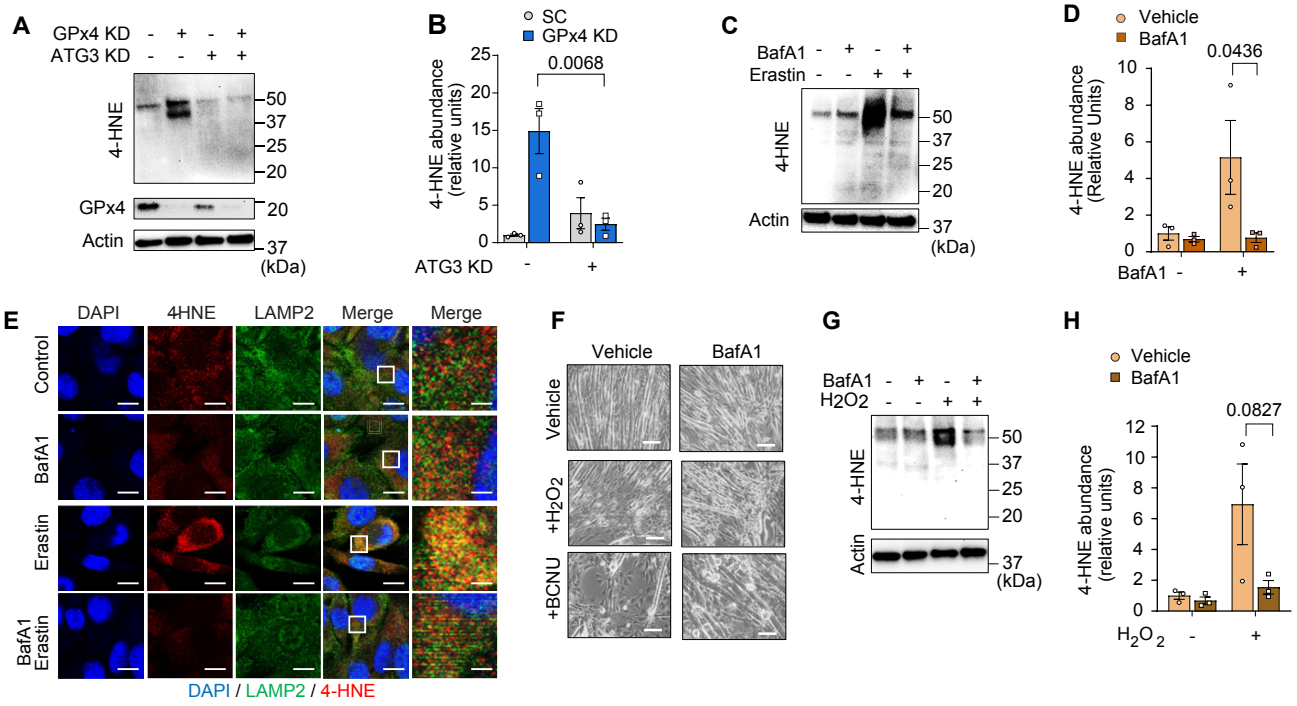
A
GPx4 KD - + - +
ATG3 KD - - + +
4-HNE
GPx4
Actin
50
37
25
20
20
37
(kDa)
B
SC
GPx4 KD
4-HNE abundance (relative units)
0.0068
ATG3 KD - +
C
BafA1 - + - +
Erastin - - + +
4-HNE
Actin
50
37
25
20
37
(kDa)
D
Vehicle
BafA1
0.0436
4-HNE abundance (Relative Units)
BafA1 - +
E
DAPI
4HNE
LAMP2
Merge
Merge
Control
BafA1
Erastin
BafA1 Erastin
DAPI / LAMP2 / 4-HNE
F
Vehicle
BafA1
Vehicle
+H2O2
+BCNU
G
BafA1 - + - +
H2O2 - - + +
4-HNE
Actin
50
37
25
20
37
(kDa)
H
Vehicle
BafA1
0.0827
4-HNE abundance (relative units)
H2O2 - +

Figure 7

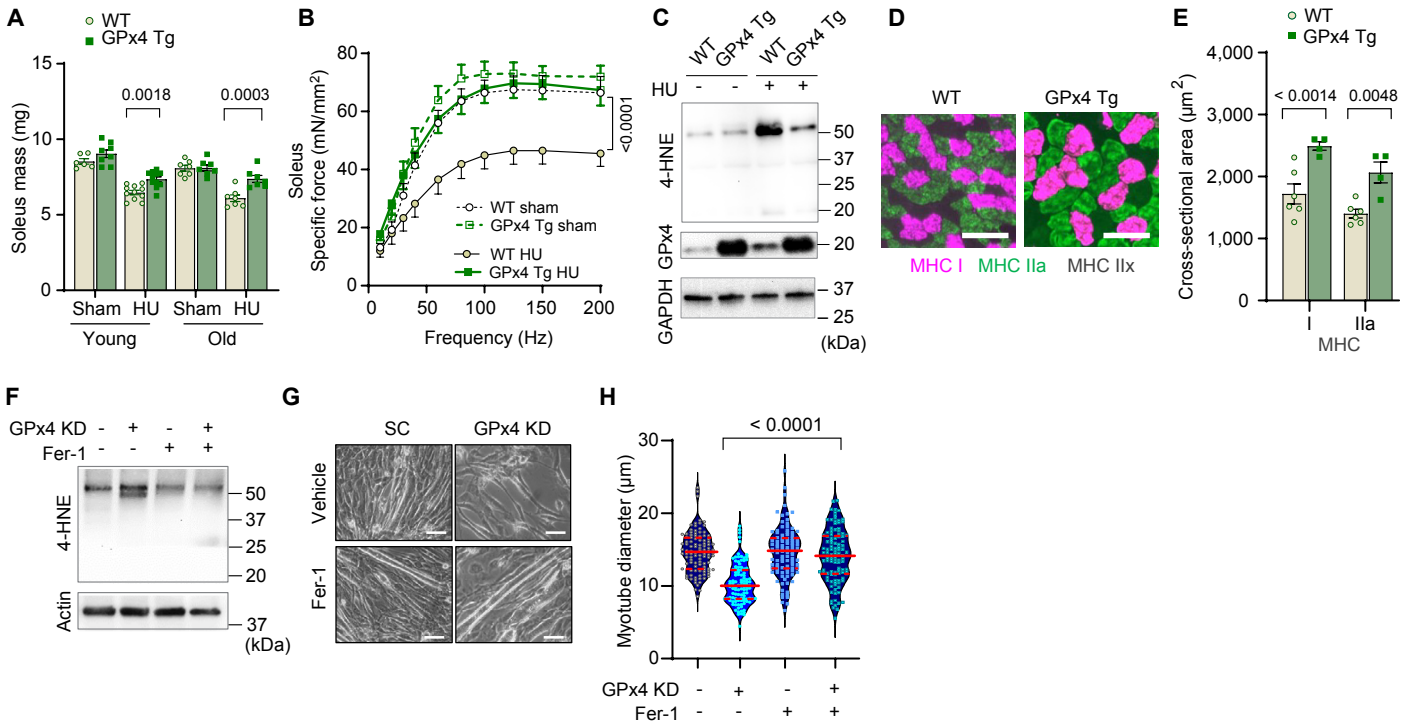
A
WT
GPx4 Tg
Soleus mass (mg)
0.0018
0.0003
Sham
HU
Sham
HU
Young
Old
B
Soleus Specific force (mN/mm²)
<0.0001
WT sham
GPx4 Tg sham
WT HU
GPx4 Tg HU
Frequency (Hz)
C
WT
GPx4 Tg
WT
GPx4 Tg
HU
4-HNE
GPx4
GAPDH
(kDa)
D
WT
GPx4 Tg
MHC I
MHC IIa
MHC IIx
E
WT
GPx4 Tg
Cross-sectional area (μm²)
< 0.0014
0.0048
I
IIa
MHC
F
GPx4 KD
Fer-1
4-HNE
Actin
(kDa)
G
SC
GPx4 KD
Vehicle
Fer-1
H
< 0.0001
Myotube diameter (μm)
GPx4 KD
Fer-1

Figure 8

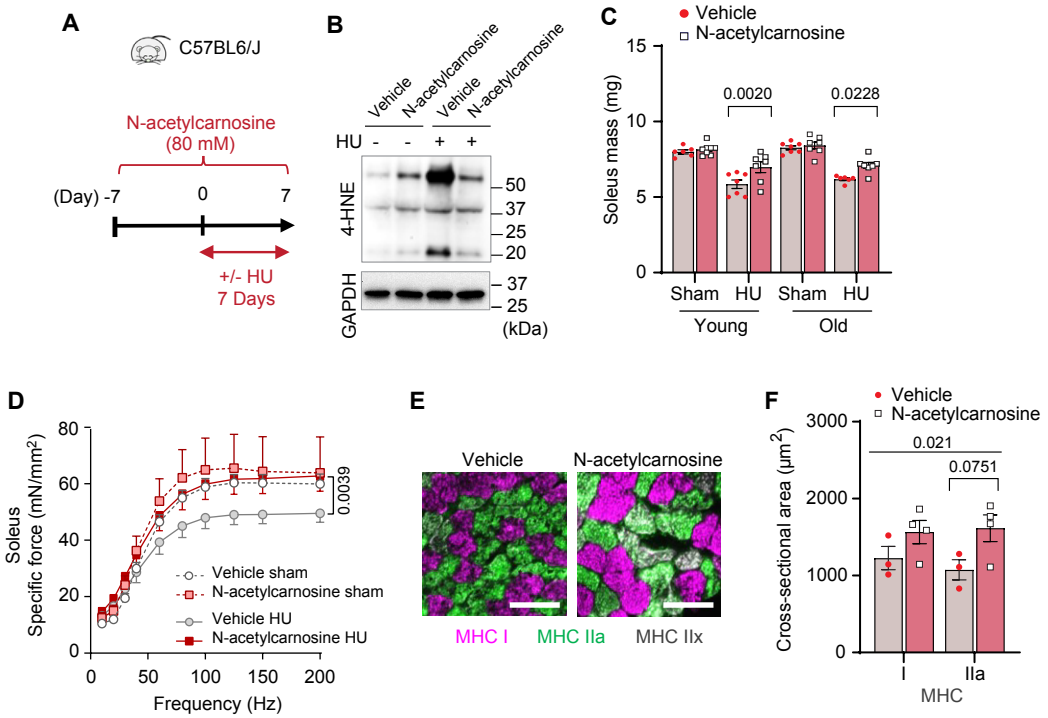
A
C57BL6/J
N-acetylcarnosine
(80 mM)
(Day) -7
0
7
+/- HU
7 Days
B
Vehicle
N-acetylcarnosine
Vehicle
N-acetylcarnosine
HU - - + +
4-HNE
GAPDH
50
37
25
20
37
25
(kDa)
C
Vehicle
N-acetylcarnosine
Soleus mass (mg)
15
10
5
0
0.0020
0.0228
Sham
HU
Sham
HU
Young
Old
D
Soleus
Specific force (mN/mm²)
80
60
40
20
0
0.0039
Vehicle sham
N-acetylcarnosine sham
Vehicle HU
N-acetylcarnosine HU
0
50
100
150
200
Frequency (Hz)
E
Vehicle
N-acetylcarnosine
MHC I
MHC IIa
MHC IIx
F
Vehicle
N-acetylcarnosine
Cross-sectional area (μm²)
3000
2000
1000
0
0.021
0.0751
I
IIa
MHC

Figure 9

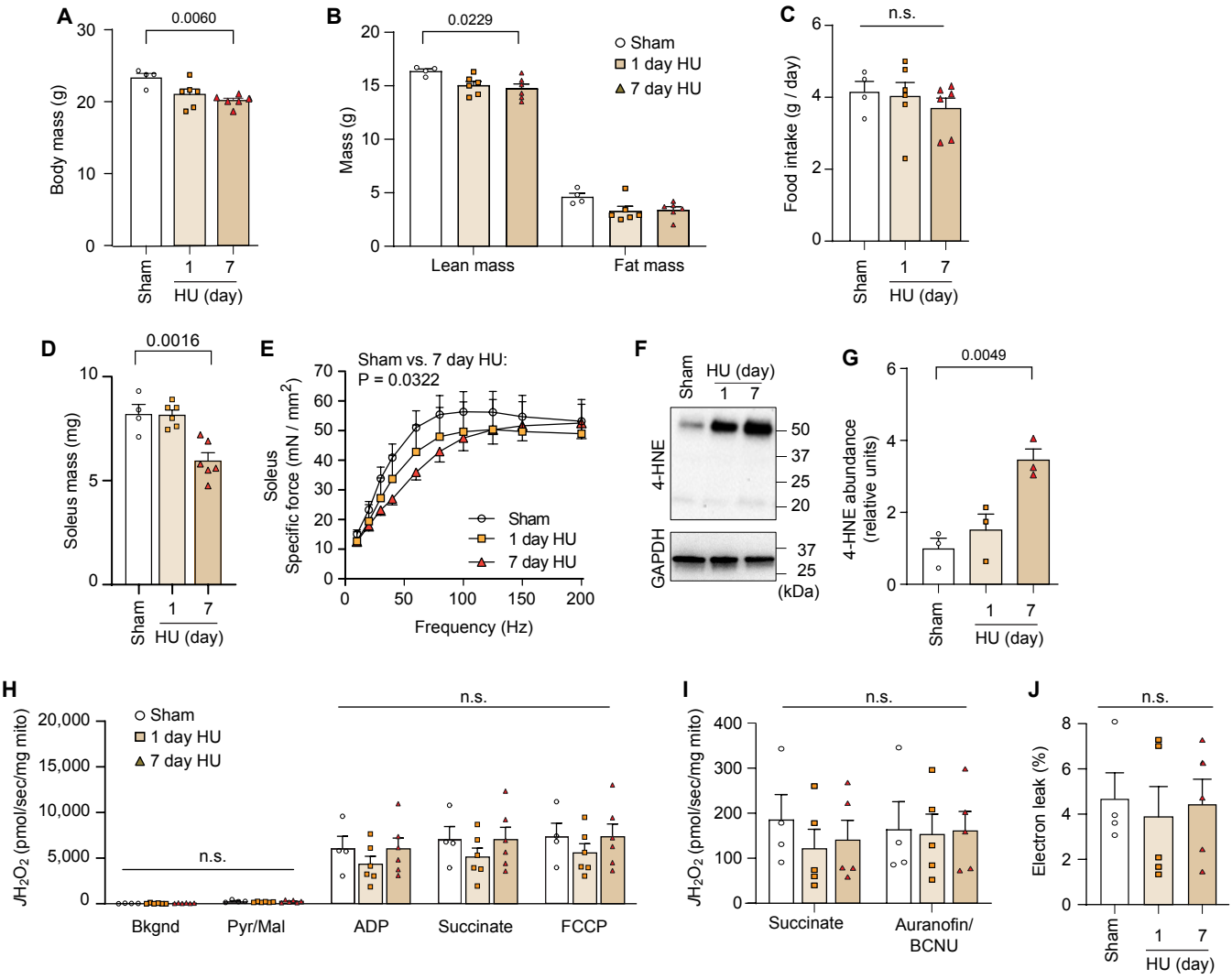

Supplemental Figure S1

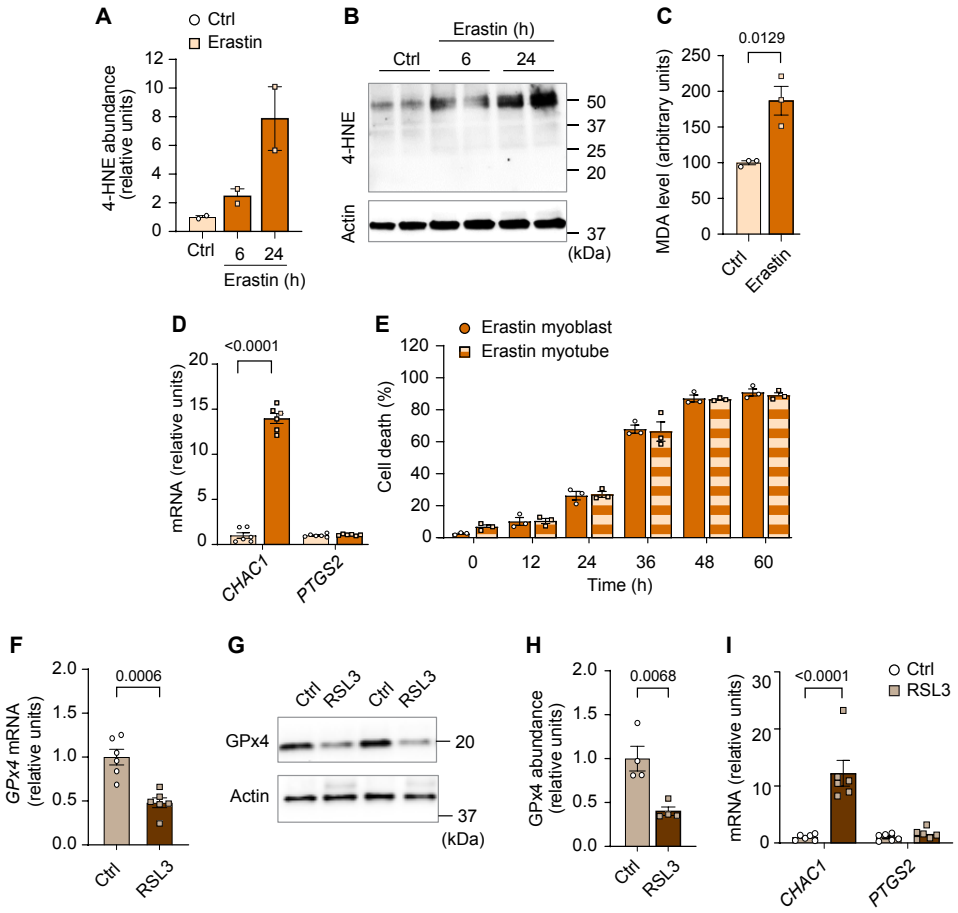

Supplemental Figure S2

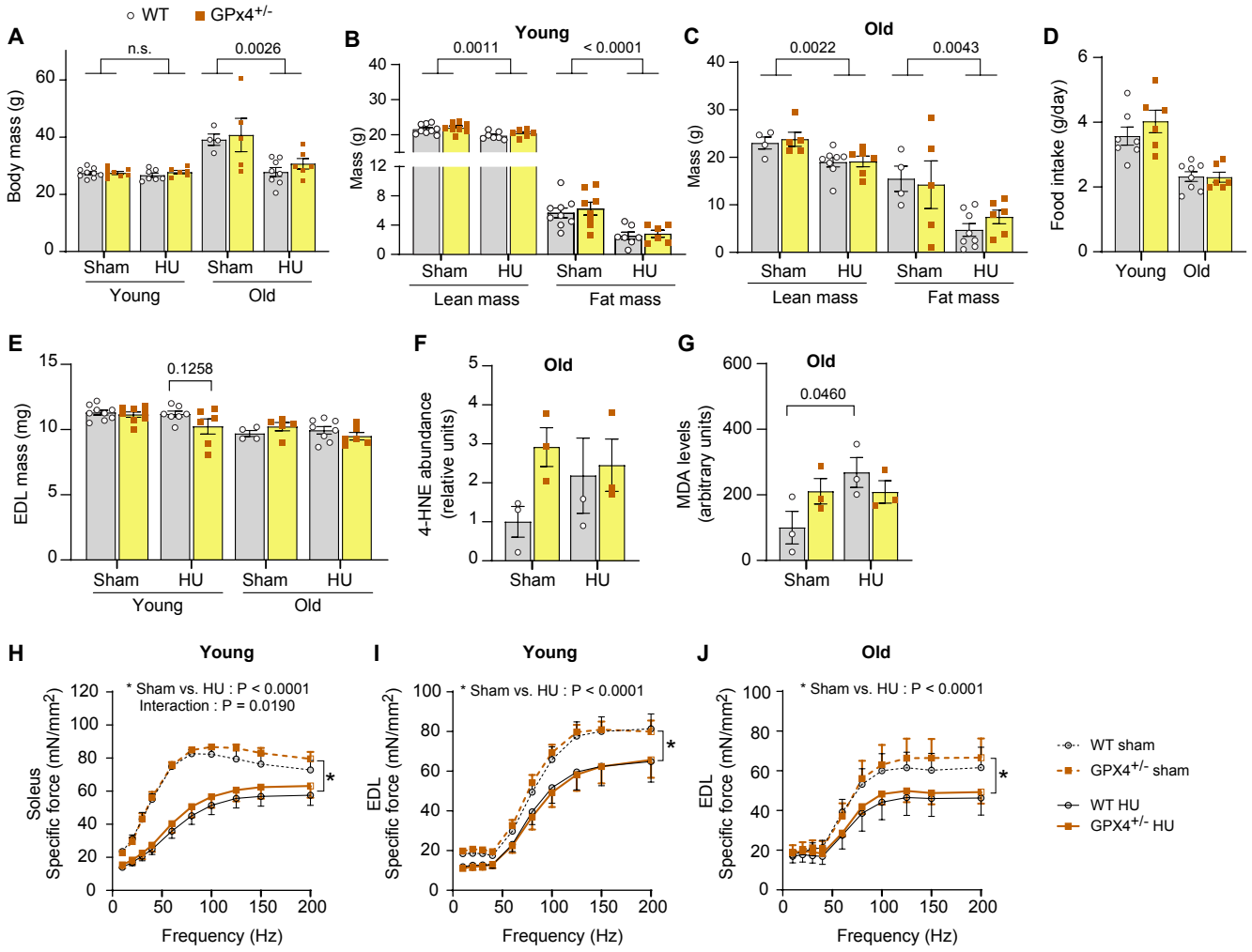

Supplemental Figure S3

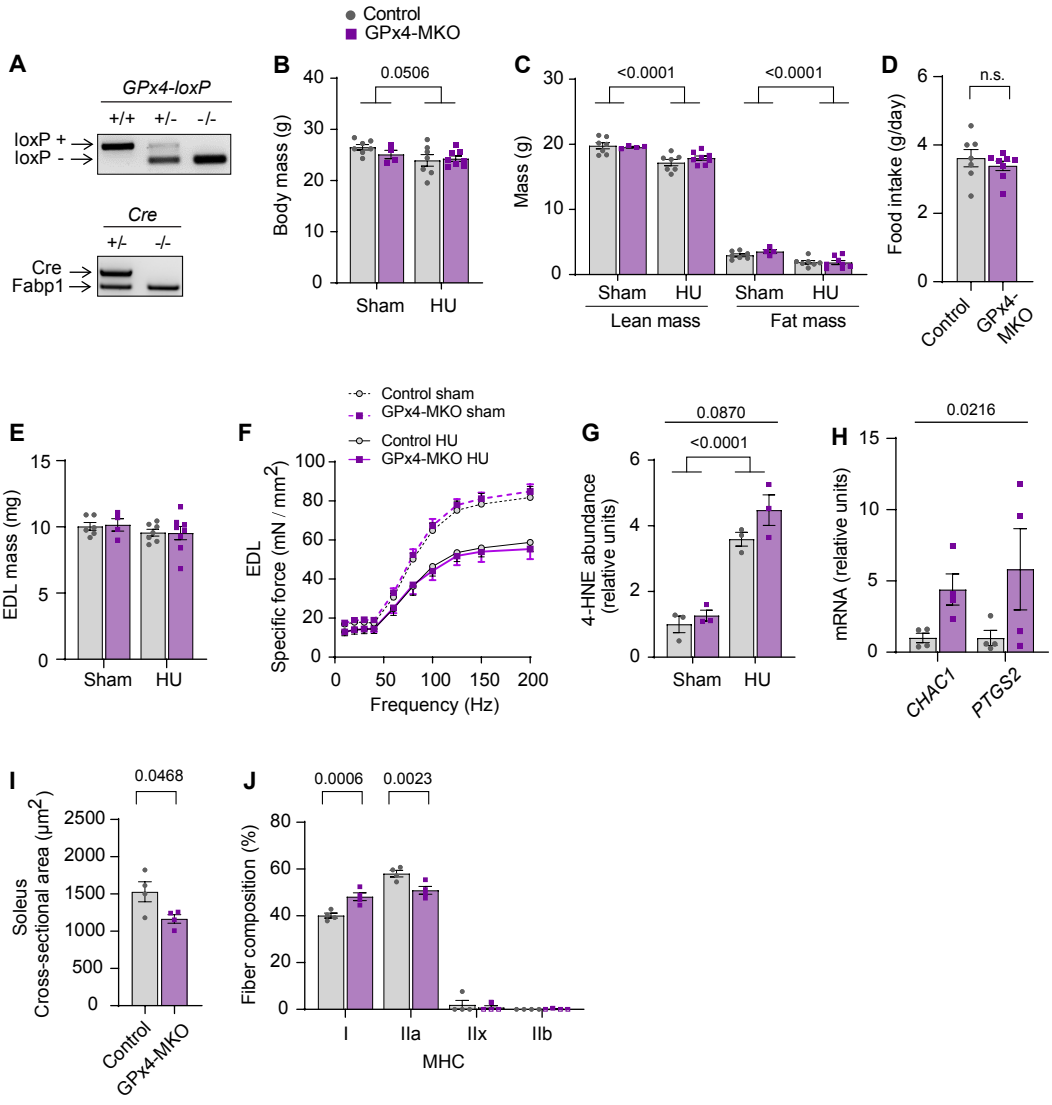

Supplemental Figure S4

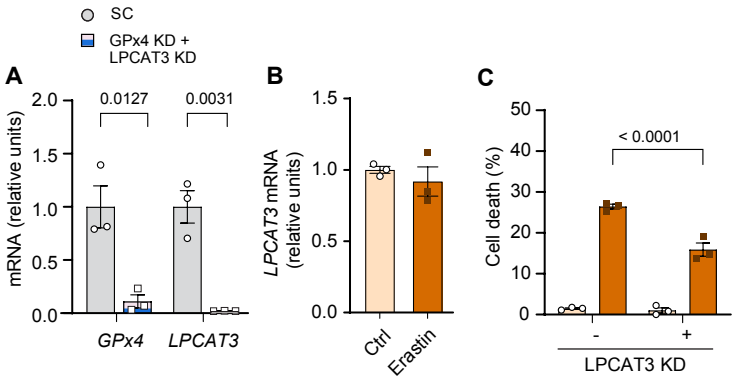

Supplemental Figure S5

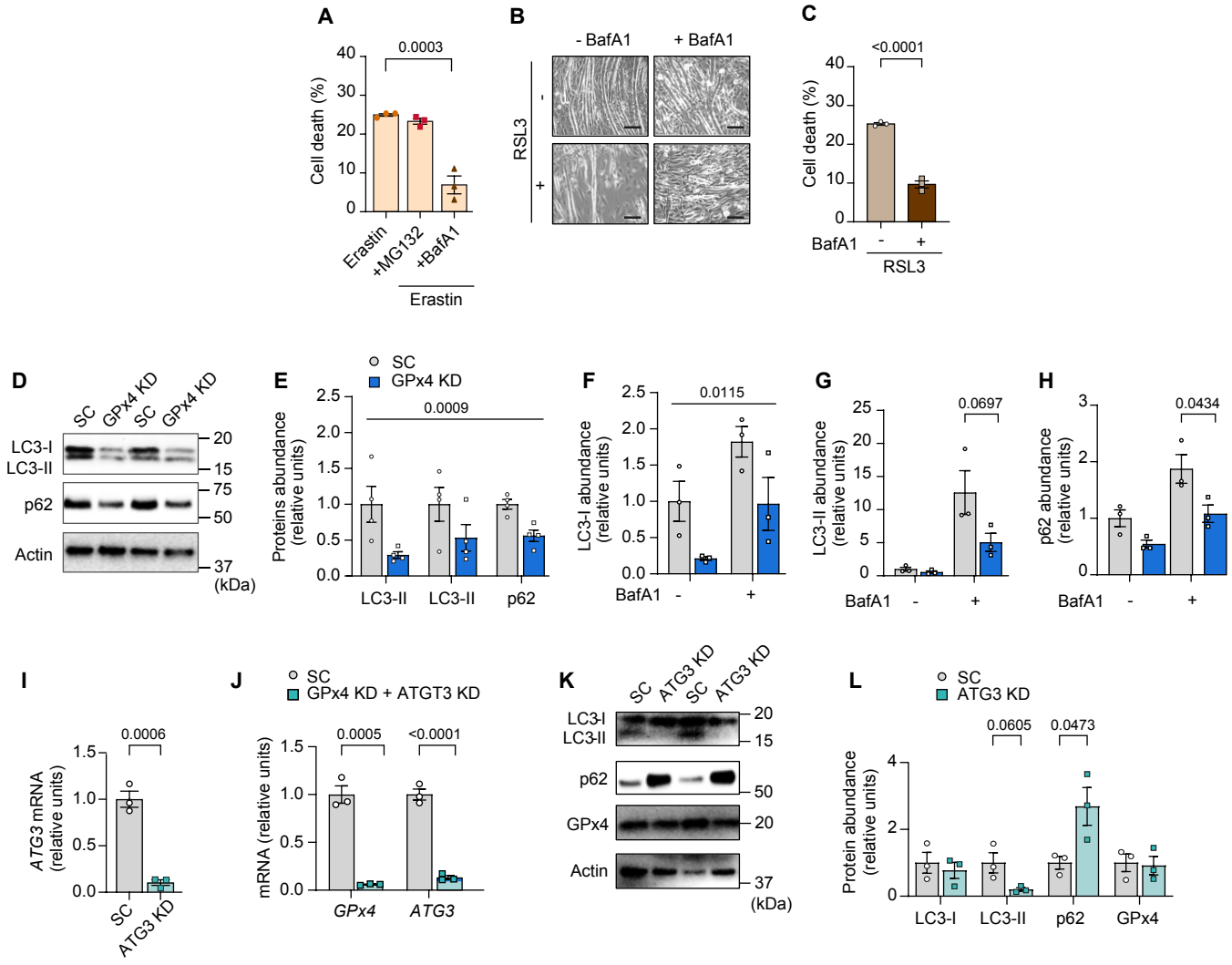

Supplemental Figure S6

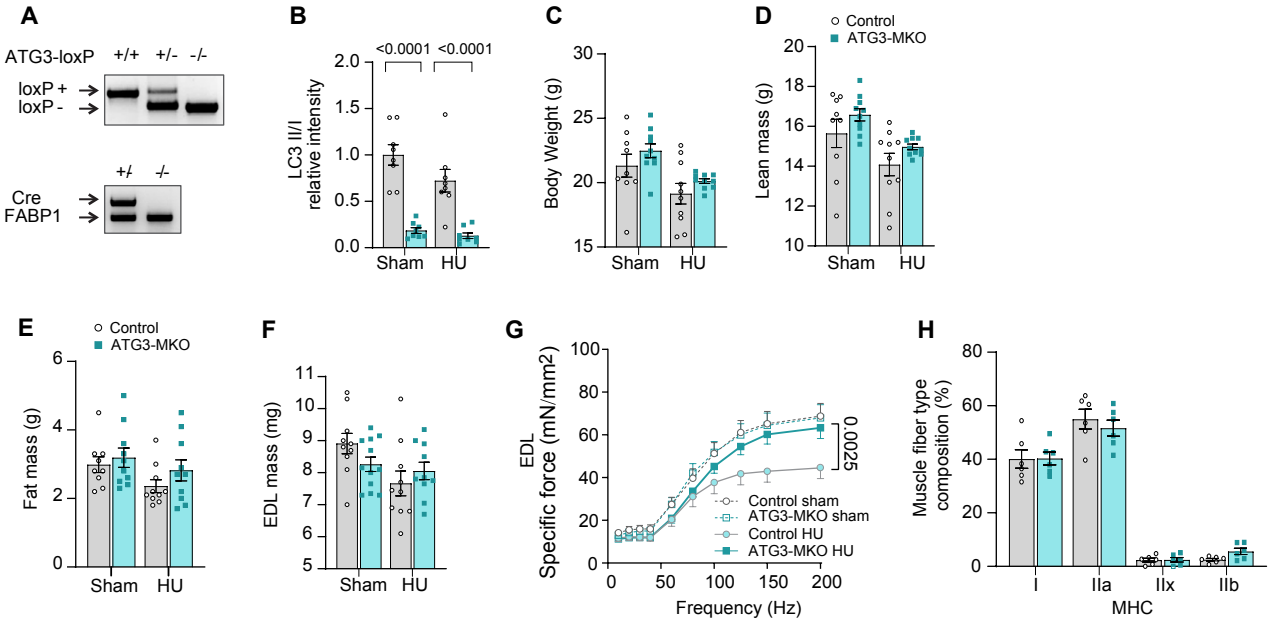

Supplemental Figure S7

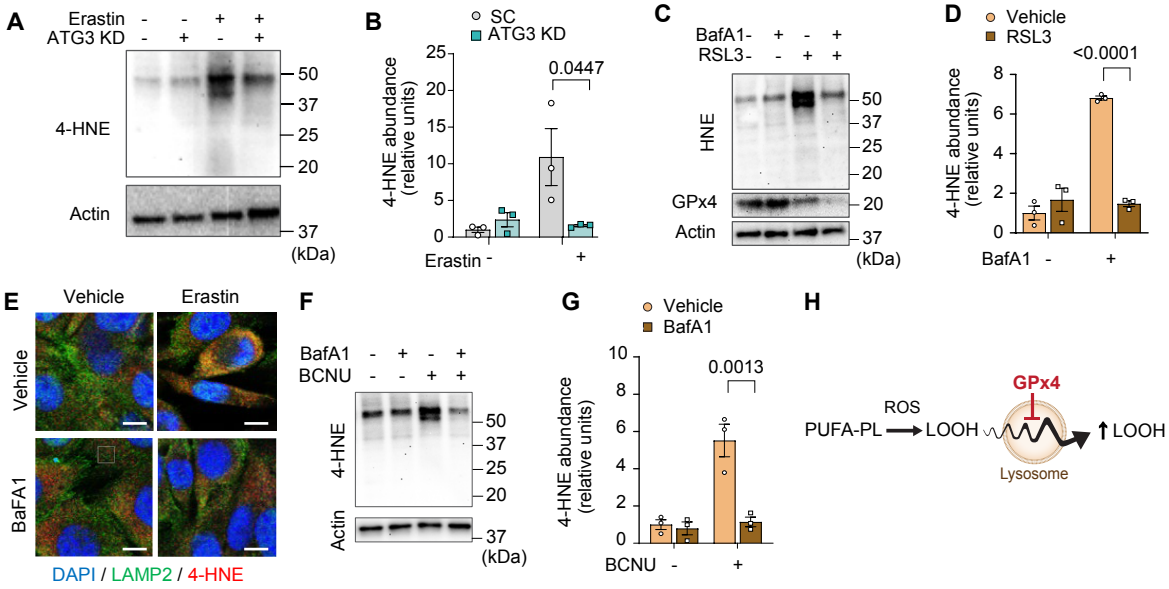

Supplemental Figure S8

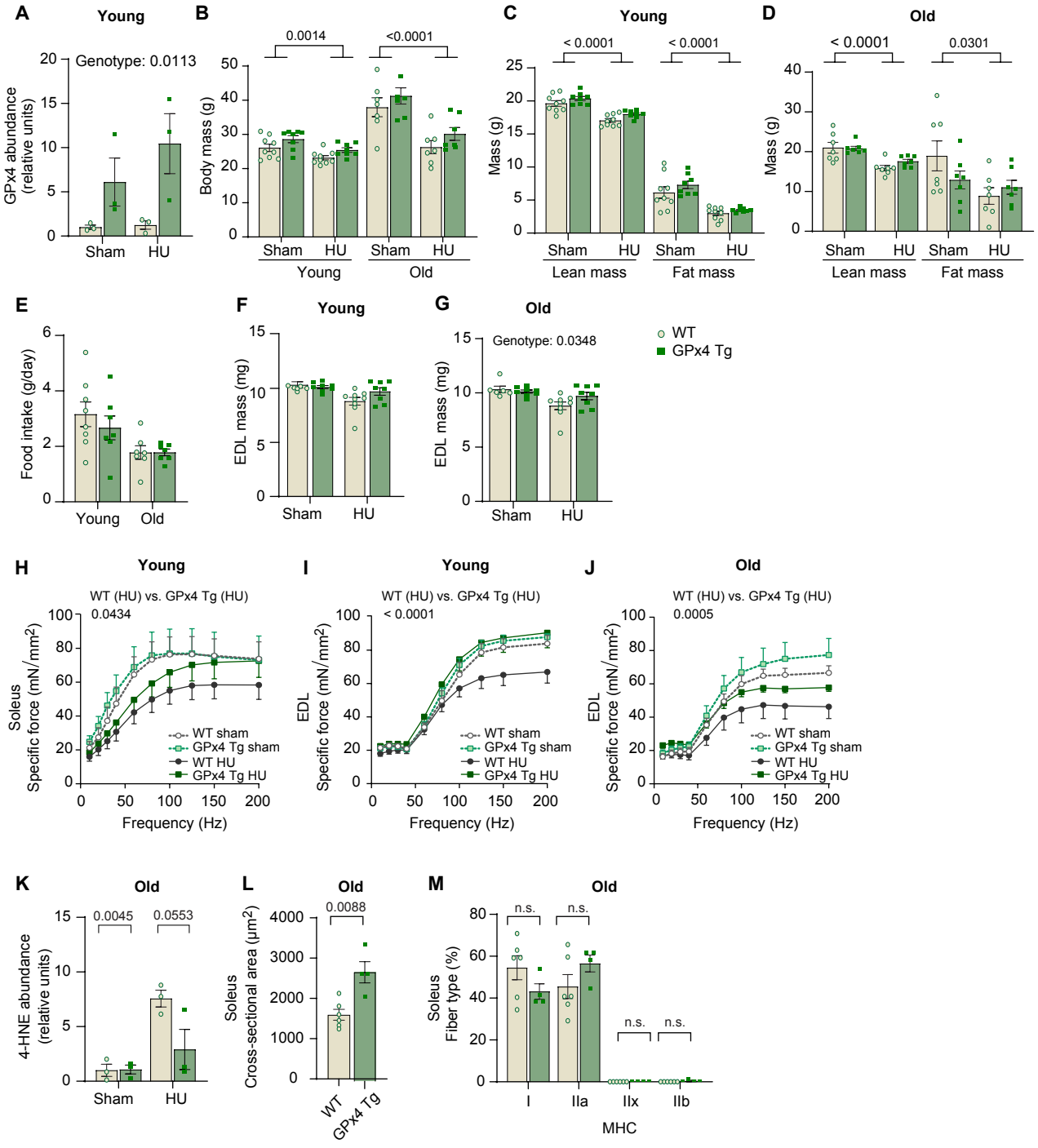

Supplemental Figure S9

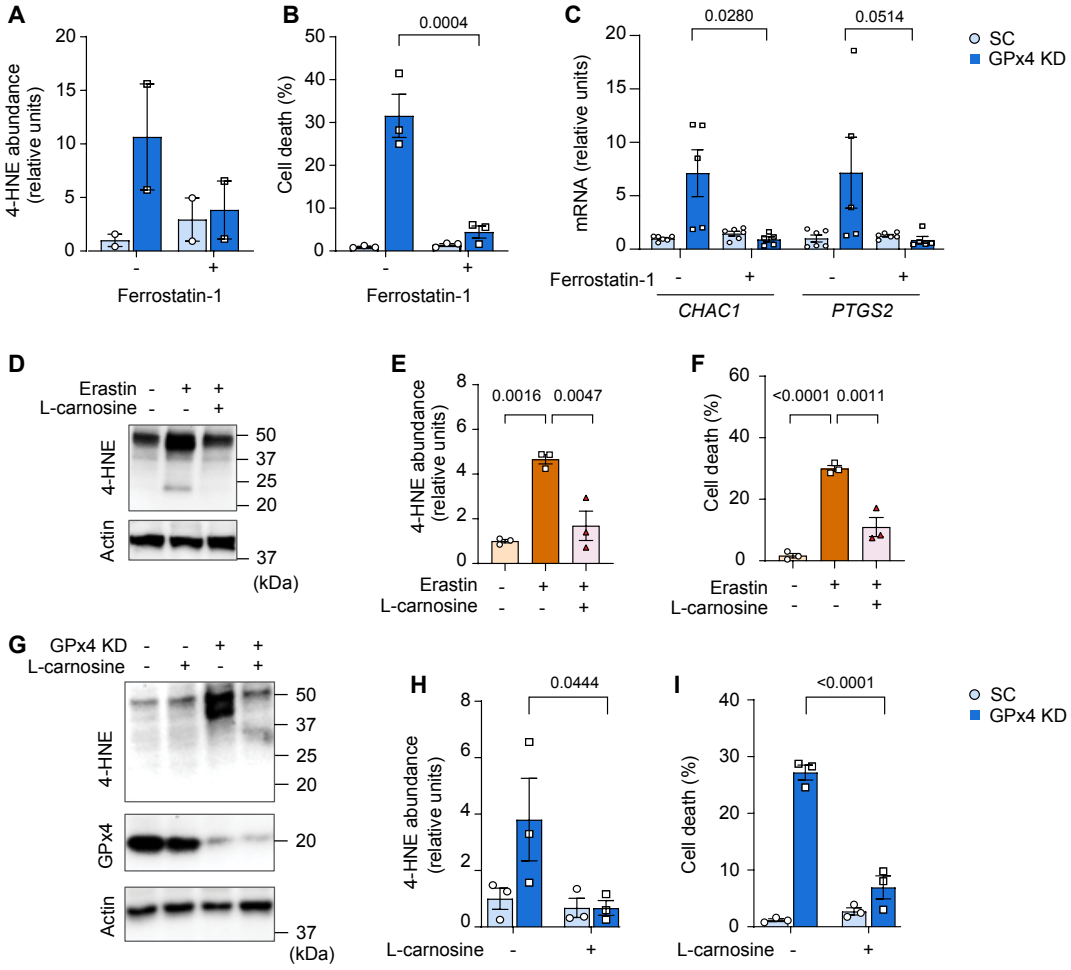
A
4-HNE abundance (relative units)
Ferrostatin-1
B
Cell death (%)
0.0004
Ferrostatin-1
C
mRNA (relative units)
0.0280
0.0514
Ferrostatin-1
CHAC1
PTGS2
SC
GPx4 KD
D
Erastin
L-carnosine
4-HNE
Actin
(kDa)
E
4-HNE abundance (relative units)
0.0016
0.0047
Erastin
L-carnosine
F
Cell death (%)
<0.0001
0.0011
Erastin
L-carnosine
G
GPx4 KD
L-carnosine
4-HNE
GPx4
Actin
(kDa)
H
4-HNE abundance (relative units)
0.0444
L-carnosine
I
Cell death (%)
<0.0001
L-carnosine
SC
GPx4 KD

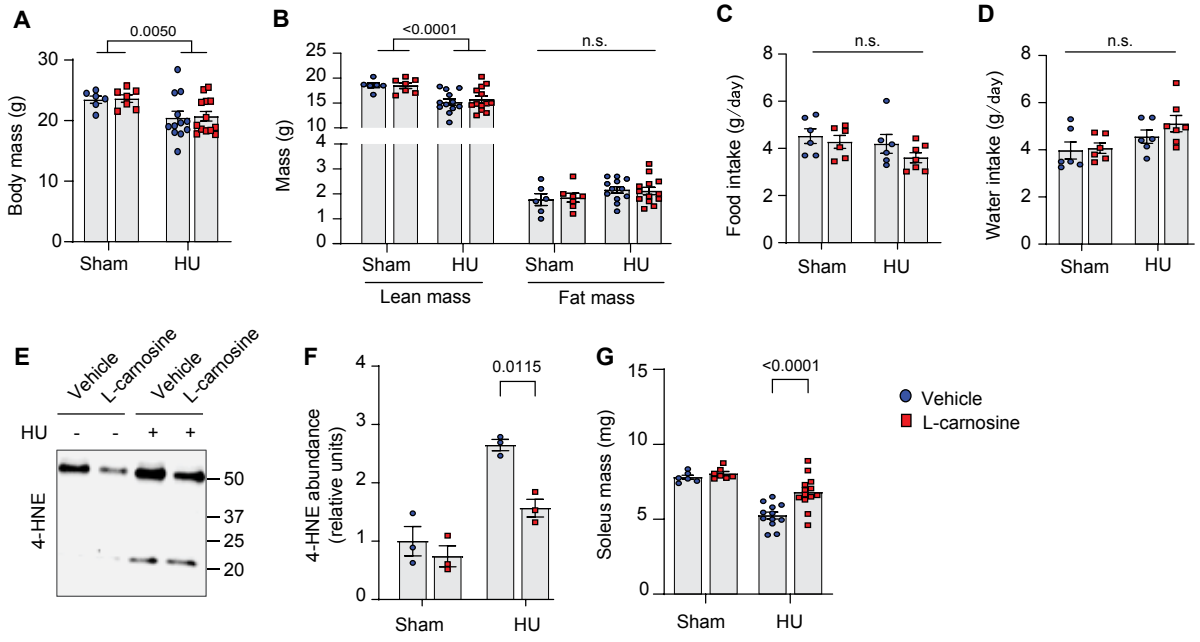

Supplemental Figure S11

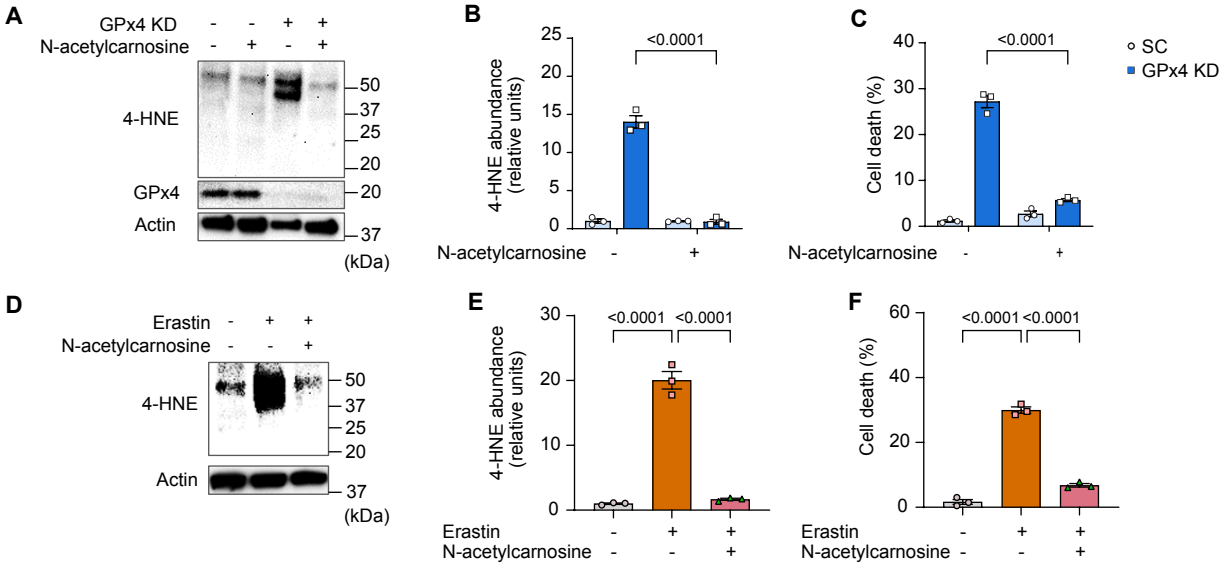

Supplemental Figure S12

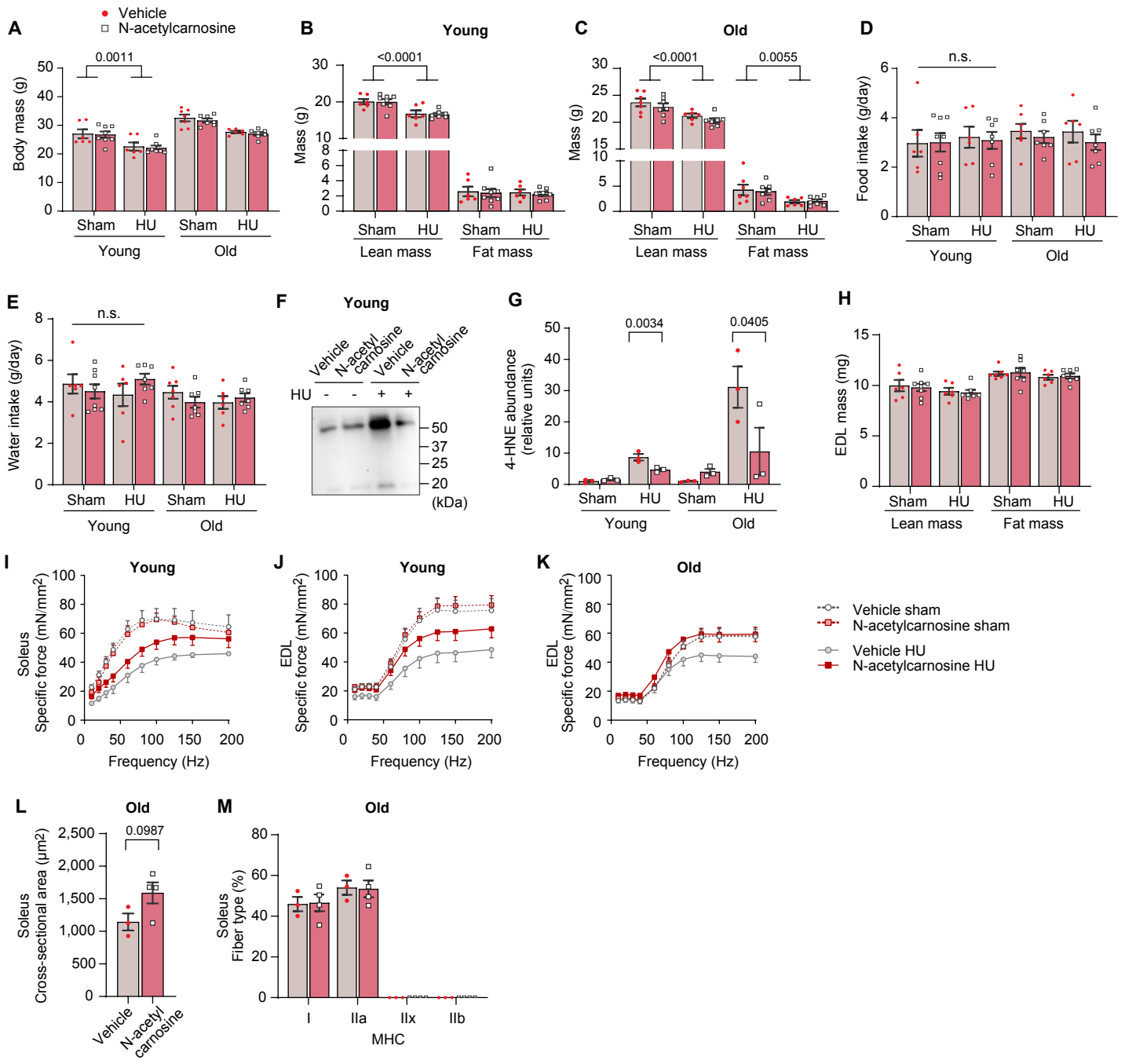

Supplemental Figure S13